Chapter 1

Solar Missions 2000-2015

1.1 Overview and Trends

The exploration of the solar corona has been tackled with ground-based instruments in optical and radio wavelengths before the start of the space age, which was initiated with the launch of *Sputnik* in October 1957. Besides some short-duration exploratory rocket flights, the first solar-dedicated space missions during the last century (see time line in Fig. 1.1) started with the satellite series of *Orbiting Solar Observatory OSO-1* to *OSO-8* (1962-1975), *Skylab* (1973-1974), the *Geostationary Operational Environmental Satellites (GOES)* series (1974-present), the *Solar Maximum Mission (SMM)* (1980-1989), the *Compton Gamma-Ray Observatory (CGRO)* (1991-2000), the *Yohkoh* mission (1992-2000), the *CORONAS-I* mission (1994-2001), *CORONAS-F* (2001-2005), *CORONAS-Photon* (2009), the *Solar and Heliospheric Observatory (SOHO)* (1996-present), and the *TRACE* mission (1998-2010). These missions expanded our view of the Sun into extreme-ultraviolet, soft X-ray, hard X-ray, and gamma-ray wavelengths and were all very successfull in providing large solar datasets and new insights into the physics of the solar corona. The theory and observational results of the physics of the solar corona obtained during the last century has been described in detail in Volume 1 (Aschwanden 2004a, *"Physics of the Solar Corona. An Introduction"*).

In this Volume 2 we are going to synthesize in the same sytematic way new theoretical and observational results that were obtained during the beginning of this millenium, covering the era of the *Ramaty High Energy Solar Spectroscopic Imager (RHESSI)* mission (2002-present), the *CORONAS-F* mission (2001-2005), the *Solar Terrestrial Relations Observatory (STEREO)* mission (2006-present), the *Hinode* mission (2006-present), the *CORONAS-FOTON* mission (2009), and the *Solar Dynamics Observatory (SDO)* mission (2010-present), (see time line in Fig.1.1). The material described in this Volume 2 is mostly based on the literature in solar physics that has been published during the mew millenium, which comprises about $\approx 12,000$ refereed publications during 2000-2012. A solar literature reference matrix classified by solar phenomena versus physical processes is provided on one of the author's webpages[1].

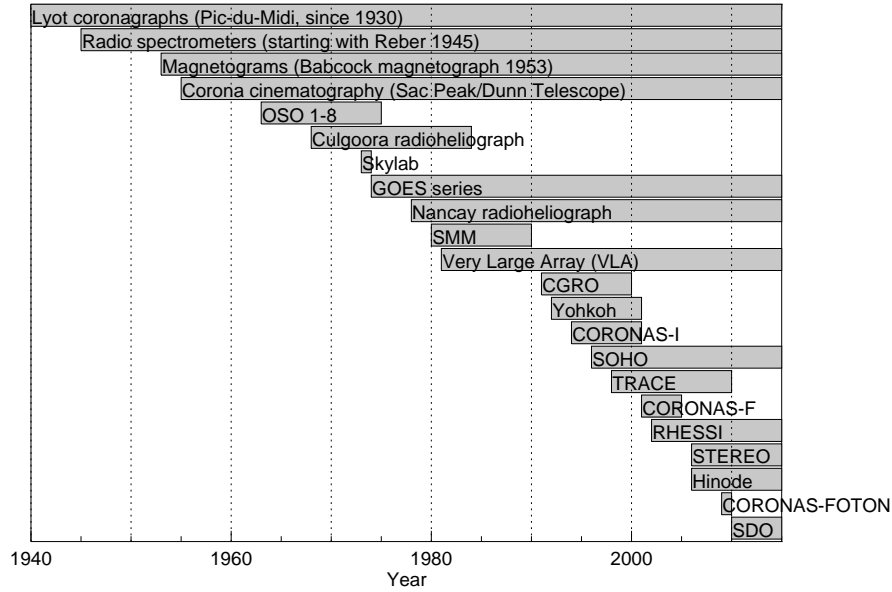[1] http://www.lmsal.com/~aschwand/publications/index.html

Figure 1.1: The operation periods of major ground-based instruments and solar-dedicated space missions during the era of 1940-2015. Note that a number of solar missions are still fully functional at the time of writing (SOHO, RHESSI, STEREO, Hinode, SDO).

Progress in solar physics during the last decades is clearly driven by new space-based and ground-based instruments that produce massive floods of imaging data, with increasingly higher spatial resolution, time cadence, and spectral resolution. *Moore's law*, which states that the number of transistors on integrated circuits doubles approximately every two years, as it has been observed over the history of computing hardware ($\approx 1970 - 2010$), obviously dominates also electronic computers and instrumental hardware in solar physics, as it can be illustrated by the exponential increase of hard drive disk capacity over the last decades (Fig. 1.2). The exponential increase in computer power enhances not only the cadence, resolution, and volume of solar imaging data, but allows us also to conduct more powerful data analysis of massive solar data sets using automated image processing techniques and feature recognition (Aschwanden 2010), as well as to perform high-powered computer simulations of solar and astrophysical plasma physics. For instance, the SDO feeds our solar data archives with a downlink data rate of 1.5 Terabyte a day, producing a staggering data flow of about one (4K $\times$ 4K) full-Sun image per second, taken in 10 different wavelength bands, compared with one image (2K $\times$ 2K) every third minute from STEREO, or one (1K $\times$ 1K) image every 12 minutes from SOHO.

The space era enabled us to explore the Sun in all wavelengths that are absorbed by the Earth's atmosphere, especially in EUV, soft X-rays, hard X-rays, and gamma-rays. Access to these wavelengths is extremely important for solar and astrophysical observations, because they allow us to detect thermal or non-thermal bremsstrahlung
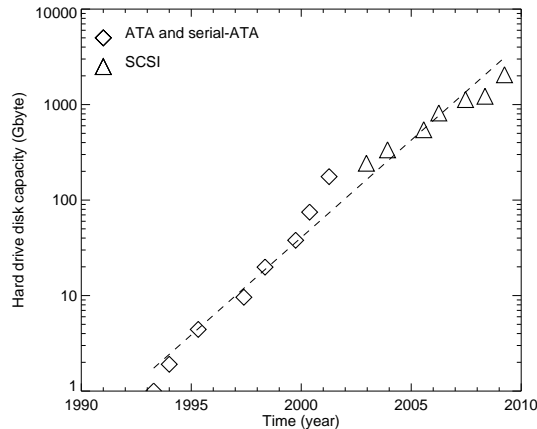
Figure 1.2: A modern version of Moore's law applied to the computer disk capacity (in Giga-bytes) as a function of time (courtesy of J.B. Gurman).

emission, as well as nuclear gamma-ray line emission, which are all manifestations of high-temperature plasmas and high-energy particles. Without space-borne detectors in those wavelength regimes, we would have no way to explore magnetic reconnection or particle acceleration in astrophysical plasmas, two key processes that control the plasma dynamics of our universe.

A key factor that distinguishes solar from stellar physics is the adequacy of spatial resolution of imaging instruments. One of the highest spatial resolutions is achieved with the *Solar Optical Telescope (SOT)* onboard Hinode, which has an angular res-olution of $\approx 0.2''$, which corresponds to ≈ 150 km on the surface of the Sun. The *Atmospheric Imaging Assembly (AIA)* onboard SDO images the full Sun with an an-gular resolution of $\approx 1.5''$ (≈ 1000 km), which corresponds to about the distance that a coronal Alfvén wave travels in 1 s. This allows us to track and reconstruct coronal MHD waves with unprecedented clarity. Solar flares are produced by magnetic recon-nection regions covering spatial scales of typically $1000 - 100,000$ km, which can be probed with AIA in great detail.

The success of solar physics, of course, should not be measured only by the new technical capabilities, but more importantly, ought to be reflected in the quality and quantity of new published results. In order to give a glance on this aspect we plot the rate of peer-reviewed publications in solar physics over the last century in Figure 1.3 (Aschwanden 2010). This histogram was obtained from annual searches for solar papers in NASA's *Astrophysical Database System (ADS)*.[2] The histogram shown in Figure 1.3 contains an estimated $\approx 32,000$ (refereed) solar publications during the time interval of $1900-2012$. Interestingly, the publication rate was extremely constant before 1950, with a leasurely average of ≈ 50 papers per year, while it suddenly started to grow afterward with an average increase of ≈ 13 papers per year, a trend that already lasts for six decades. Note also a remarkable spike after 1967, when the journal *Solar*
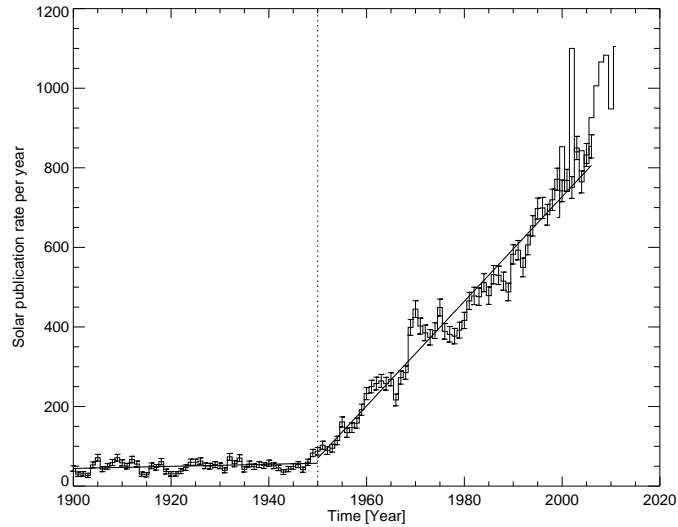
---

[2]http://adsabs.harvard.edu/

Figure 1.3: The rate of publications in solar physics over the last century, based on NASA's Astronomical Database System (ADS). The publications after 2000 (histogram without error bars) have been identified each by individual inspection and classification of solar content. Linear regression fits indicate an almost constant rate of ≈ 50/year before 1950, while the rate increases linearly after the beginning of the computer and space age (adapted from Aschwanden 2010).

Physics was founded. Technological and economical conditions definitely improved to such a degree after 1950 that productivity in science rapidly accelerated. If we compare the progress in computer technology according to Moore's Law shown in Figure 1.2, we note that data storage and processing capacity grew exponentially after 1960, while science results measured in terms of publications grew linearly after 1950 (Figure 1.3), so we may conclude that science return scales approximately logarithmically with the amount of available data. This is an important lesson that underscores the need for automated data processing methods in order to keep up with current growth in science return.

In the following subsections we describe the science goals and technical capabilities of the new space missions that came along after 2000, which includes RHESSI (Section 1.2), STEREO (Section 1.3), Hinode (Section 1.4), SDO (Section 1.5), the CORONAS missions (Section 1.6), and other space missions, suborbital rocket flights, and balloon flights (Section 1.7). For completeness we give also an overview of solar instruments in radio wavelengths (Section 1.8) and optical or infrared wavelengths (Section 1.9) that were active during the last decade.
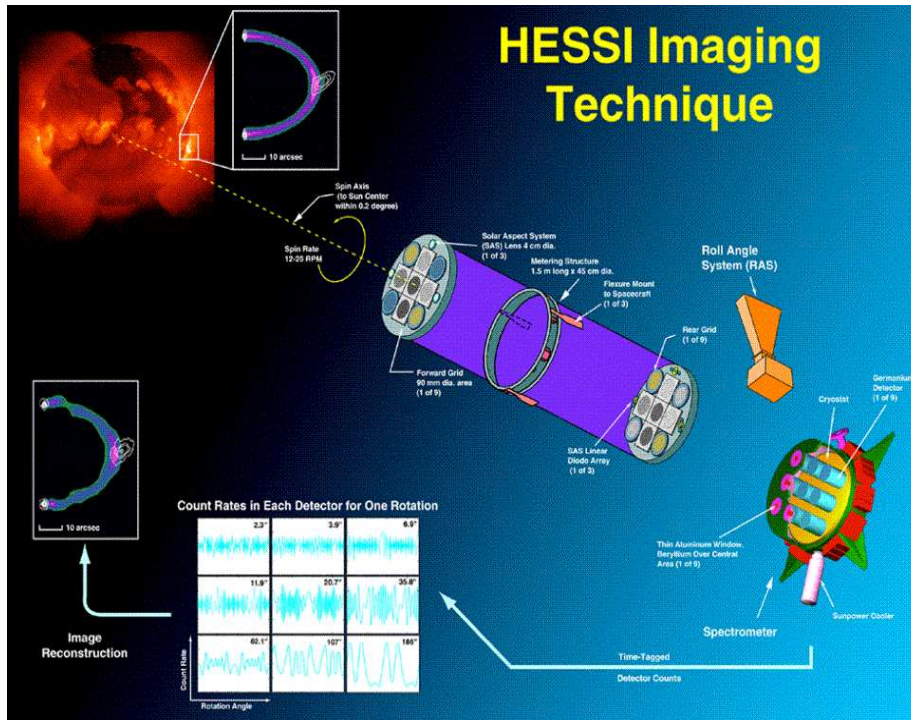
Figure 1.4: Imaging Technique of the RHESSI instrument (courtesy of NASA/GSFC).

1.2 The RHESSI Mission

The *Reuven Ramaty High Energy Solar Spectroscopic Imager (RHESSI)*[3] instrument is a rotation-modulated hard X-ray Fourier-type imager, a solar-dedicated space mission that was launched on 2002 February 5, and is still operational at the time of writing. RHESSI's primary mission is to explore the basic physics of particle acceleration and explosive energy release in solar flares. This is achieved through imaging spectroscopy in X-rays and gamma-rays with fine angular and energy resolution to reveal the locations and spectra of the accelerated electrons and ions and of the hottest flare plasma.

The working principle of the RHESSI instrument is illustrated in Figure 1.4: The spin-stabilized spacecraft carries an instrument that consists of nine subcollimators with grids of variable widths, which transmit soft and hard X-ray photons in form of nine modulated time profiles, which can be processed into two-dimensional images using Fourier transform methods. The grid spacings vary from $2.3''$ to $\gtrsim 3'$ in steps of $\sqrt{3}$, allowing sources to be imaged over a wide range of angular scales, from the sizes of flare loop footpoint diameters to sizes of entire active regions. The energy range spans from 3 keV to 17 MeV, where the energy resolution is $\lesssim 1$ keV at 3 keV, and increases to ≈ 5 keV at 5 MeV, thanks to the technology of germanium-cooled detectors. This high energy resolution allows RHESSI to resolve essentially all solar

---

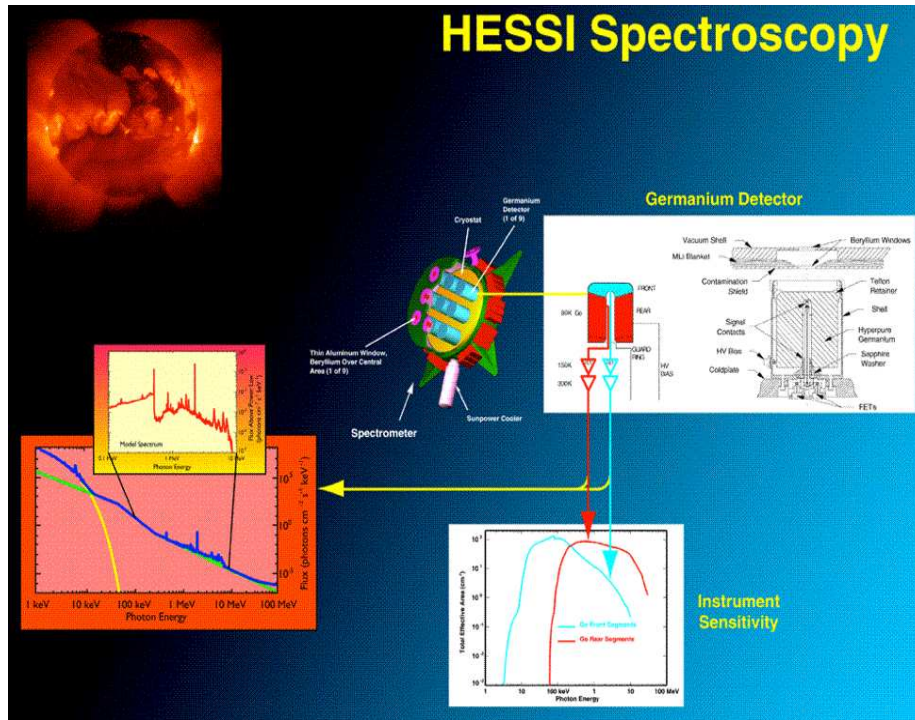[3]http://hesperia.gsfc.nasa.gov/rhessi2/

Figure 1.5: Spectroscopy of the RHESSI instrument (courtesy of NASA/GSFC).

gamma-ray lines for the first time. An automated shutter system allows a wide dynamic range ($> 10^7$) of flare intensities to be handled without instrument saturation. Data for every photon is stored temporarily in a solid-state memory, before telemetered to the ground control center at the University of Berkeley, which allows post-event selection of time intervals with higher data rates. The spin rate of the satellite is one rotation per 4 s, which allows a basic time resolution of 2 s, or higher if a light curve demodulation technique is employed. The rotational modulation of the hard X-ray collimators allows us to obtain many more Fourier components of the image than the 9 basic components of the subcollimators, and thus yields finer details in the reconstructed images.

Technical descriptions of the RHESSI instrument are provided in pre-launch documents (Dennis et al. 1996; Lin et al. 1998, 2000a,b), as well as in post-lauch documents with first results (Lin et al. 2002a,b, 2004a,b), mostly in the special issue of *Solar Physcis* volume **210** (Lin et al. 2002a). A list of instrument characteristics is given in Table 1.1. The major advances in solar hard X-ray observations provided by RHESSI are the capabilities of the first high-resolution hard X-ray imaging spectroscopy (Fig. 1.5), the first high-resolution gamma-ray line spectroscopy, and the first imaging above 100 keV, including the first imaging of gamma-ray lines (Lin et al. 2002b). Imaging with RHESSI is accomplished with the reconstruction of spatial maps based on the Fourier components measured with the rotation-modulated collimators (Hurford et al. 2002, 2003; Hurford 2003), using specific algorithms such as

Table 1.1: RHESSI Instrument Characteristics (adapted from Lin et al. 2002a).

Parameter	Characteristics
Technique:	Fourier-transform imaging with rotating modulation collimators
Angular resolution:	$2.3''$ at 100 keV, increasing to $36''$ at 15 MeV
Angular coverage:	$2'' - 180''$
Field of view:	Full Sun ($\approx 1°$)
Temporal resolution:	≈ 10 ms for coarse image, 2 s for fine image
Energy range:	3 keV to 17 MeV
Energy resolution:	< 1 keV FWHM at 3 keV, increasing to ≈ 5 keV at 5 MeV
Detectors:	9 two-segment *n*-type germanium (7.1 cm diameter times 8.5 cm), cooled to < 75 K with Stirling-cycle mechanical cooler
Effective area:	$\approx 10^{-3}$ cm^2 at 3 keV, ≈ 32 cm^2 at 10 keV (without attenuators), ≈ 60 cm^2 at 100 keV, ≈ 15 cm^2 at 5 MeV
Imager:	9 pairs of tungsten grids, with pitches from 34 μm to 2.75 mm, 1.55 m front-to-rear grid separation
Aspect system:	Sensor Aspect System (SAS) for Sun direction $< 1.5''$ Roll Aspect System (RAS) for roll angle $< 3'$
Spacecraft spin rate:	15 rpm, pointing to $0.2°$ of Sun center
Spacecraft mass:	291.1 kg
Spacecraft power:	220.4 W
Spacecraft size:	1.18 m diameter, 2.06 m height, 5.74 m solar panel span
Telemetry:	4 Mbps, downlink
On-board storage:	4 Gbyte solid state memory
Launch vehicle:	Pegasus XL
Launch date:	2002 February 5
Orbit:	$38°$ inclination, 587-600 km altitude

back-projection methods, *Clean iterations*, *maximum entropy methods (MEM)* (Sato 2002), *pixon reconstruction* (Metcalf et al. 1996), *forward-fitting methods* to modulated time profiles (Aschwanden et al. 2002c) or to *uv-Fourier component visibilities*. Since RHESSI is a spinning spacecraft with a period of ≈ 4 s, time profiles with finer time bins require a demodulation of the RHESSI count rates (Arzner 2002, 2004a,b). Nutation of the spinning spacecraft can also lead to instrumental oscillations in RHESSI count rates with periods of ≈ 75 s (Inglis et al. 2011).

Spectroscopy is carried out by inversion of the electron energy injection spectrum from the observed bremsstrahlung photon spectrum, for instance with a *regularization inversion method* (Massone et al. 2003). The sophisticated RHESSI data analysis software is described in Schwartz et al. (2002). Cross-calibration of the RHESSI instrument has been investigated by comparisons with images form TRACE (Phillips et al. 2005; Tripathi et al. 2006), EIT and CDS from SOHO (Tripathi et al. 2006), and fluxes measured with SMART-1 XSM and GOES (Väänänen et al. 2009).

RHESSI is a NASA Samll Explorer Mission, operated and controlled from the ground systems at the University of Berkeley (Bester et al. 2003). The hardware of the RHESSI spacecraft includes the 9 bi-grid collimators and the spectrometer with 9 cryogenically cooled Ge detectors (Smith et al. 2002), a beryllium (Be) scattering

element that enables hard X-ray polarimetry (McConnell et al. 2002), the *Solar Aspect System (SAS)* and a *Roll Angle System (RAS)* to control the pointing and the roll angle of the rotating spacecraft (Henneck et al. 1999a,b; Fivian et al. 2002, 2003; Fivian 2005; Zehnder et al. 2003; Hurford and Curtis 2002), and an *Instrument Data Processing Unit (IDPU)* that handles up to 40 Mbps of telemetry during solar flares (Curtis et al. 2002). An ancillary *RHESSI Experimental Data Center (HEDC)* with data archive services was also established at ETH Zürich (Saint-Hilaire et al. 2002).

Since RHESSI successfully operated more than a decade we can already list the major discoveries and new scientific breakthroughs, which have also been reviewed in the monograph *High-Energy Aspects of Solar Flares: A RHESSI-Inspired Monograph* in the Special Issue of *Space Science Review* volume **159**/1-4 (2011). A good source of novel results from RHESSI that are periodically announced can also be found on the *RHESSI Science Nuggets* webpage[4]. A subset of 10 solar and 3 non-solar iconic results that constitute RHESSI's scientific legacy have been singled out at the occasion of RHESSI's Tenth Anniversary (see RHESSI Science Nugget webpage item 169 by Dennis and Lin 2011):

1. Discovery of Gamma-Ray Footpoint Structures: In the largest solar flare observed by RHESSI, double ion footpoints have been imaged in the energy range of ≈ 2.2 MeV (dominated by gamma-ray lines), which were found to be slightly but significantly displaced from the electron precipitation sites usually seen in $\gtrsim 25$ keV hard X-rays, which poses an interesting new problem for standard particle acceleration models (Hurford et al. 2003, 2006; Smith et al. 2003).

2. Energy Content and Spectrum of Flare Energetic Electrons: The high spectral resolution of ≈ 1 keV allows unambiguously to separate the thermal (Gaussian-like) from the non-thermal (powerlaw-like) spectral component, so that the thermal and non-thermal flare energies can be determined separately, as well as including the effects of Compton backscattering (Holman et al. 2003; Kasparova et al. 2005; Kontar et al. 2006, 2011; Massone et al. 2004; Saint-Hilaire and Benz 2005; Sui et al. 2005, 2006).

3. Ubiquitous Nonthermal Emission from the Corona and Bulk energization: Nonthermal hard X-ray emission is generally detected at the footpoints of flare loops (Krucker and Lin 2008), but RHESSI detects it also at coronal heights above flare loops (Battaglia and Benz 2007; Ishikawa et al. 2011; Krucker et al. 2010), in occulted flares (Krucker and Lin 2008), in the preflare phase (Lin et al. 2003), in the absence of footpoint emission (Veronig and Brown 2004), associated with jets (Bain and Fletcher 2009), and cospatial with coronal mass ejections (Krucker et al. 2007).

4. Double Coronal X-ray Sources: RHESSI detected double hard X-ray sources in some limb flares, with a vertically symmetric energy gradient below and above a supposed X-point reconnection site (Sui and Holman 2003; Liu et al. 2008).

---

[4]http://sprg.ssl.berkeley.edu/~tohban/wiki/index.php/RHESSI_Science_Nuggets

5. <u>Microflares:</u> RHESSI registered hard and soft X-rays from over 25,000 microflares, distributed evenly in the northern and southern mid-latitude band, associated with active regions, which supports the conclusion that they do not heat the quiet corona (Benz and Grigis 2002; Krucker et al. 2002; Christe et al. 2008; Hannah et al. 2007, 2008, 2010, 2011; Stoiser et al. 2007).

6. <u>Initial Downward Motion of X-ray Sources:</u> An unexpected initial downward motion of coronal hard X-ray sources was discovered in a number of flares, apparently associated with the propagation of reconnection along flare ribbons (Sui et al. 2004; Veronig et al. 2006; Ji et al. 2008).

7. <u>Hard X-Ray Flare Ribbons:</u> The chromospheric double ribbons that are often visible in EUV, UV, or white-light, are generally not seen in hard X-rays due to the limited dynamic range of Fourier imaging, but RHESSI imaged larger segments of them in some flares (Fletcher and Hudson 2002; Liu et al. 2007; Dennis and Pernak 2009; Krucker et al. 2011).

8. <u>Location of Superhot X-Ray Source:</u> Superhot ($>$30 MK) flare plasmas was detected in large coronal altitudes (even during the pre-impulsive flare phase), and is thus of coronal origin, rather than caused by chromospheric evaporation, which also generally produces a high-temperature component of ≈ 20 MK. (Caspi and Lin 2010; Caspi 2010).

9. <u>Photospheric X-ray Albedo:</u> Back-reflected hard X-ray photons from the photosphere were detected, where the solar surface acts like a *Compton mirror* (Kontar and Brown 2006).

10. <u>511-keV Positron Annihilation Line:</u> RHESSI resolved the spectral width of the 511 keV positron annihilation line, with a line width of typically $\gtrsim 5$ keV, which indicates a temperature of the accelerated-ion interaction region around $T \approx 10^5$ K, which is much higher than the expected value of $T \approx 10^4$ K in the chromosphere (Share et al. 2004).

The novel observations of RHESSI and the underlying theory will be discussed in more detail in sections 11-14 on Solar Flares. Other scientific highlights of the RHESSI mission are not related to solar flares, such as measurements of the oblateness of the Sun (Fivian et al. 2008), the discovery of a huge flare from the soft-gamma-ray repeater (SGR) 1806-20 with quasi-periodic oscillations that were interpreted as "ringing" modes of the neutron star (Hurley et al. 2005; Watts and Strohmayer 2006), and terrestrial gamma-ray flashes associated with lightenings or sprites (Smith 2005; Dwyer and Smith 2005).

1.3   The STEREO Mission

The twin *Solar TErrestrial RElations Observatory (STEREO)*[5] spacecraft were launched on 2006 October 26. At end of January 2007 the two spacecraft separated and entered
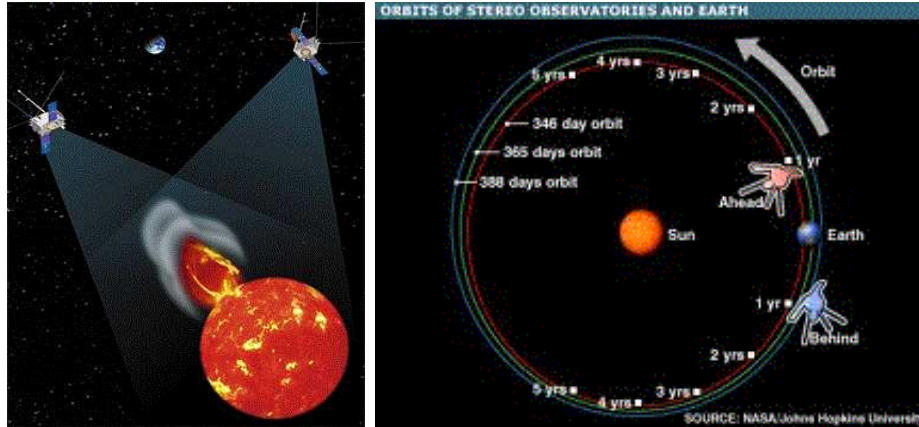
[5]http://stereo.gsfc.nasa.gov/

Figure 1.6: *Left:* Artist's concept of the STEREO twin spacecraft 3D perspective on a coronal mass ejection launched from the Sun. *Right:* Orbits of STEREO-A (red) and STEREO-B (blue) with respect to the Earth's annual orbit (green). (Credit: NASA).

heliospheric orbits in opposite directions, STEREO-A(head) leading in East direction and STEREO-B(ehind) trailing in West direction around the Sun, increasing their separation by $\approx 45°$ per year, but maintaining their average distance of $\approx 1.0 \pm 0.1$ AU from the Sun all the time (Figure 1.6). At the time of writing, the two spacecraft are separated by more than $180°$. These particular orbits provide solar data that are suitable for small-angle stereoscopy of active regions in the solar corona at the beginning of the mission (or later whenever the separation angle is near zero or 180 degrees), while large-angle stereoscopy and tomography is feasible in most later years, designed to provide the 3D reconstruction of coronal mass ejections that are launched in the solar corona and propagate through interplanetary space. Because of the varying distance of the two spacecraft from Earth, the data rate and telemetry is highest at the beginning of the mission, but drops continuously with increasing distance later in the mission. The STEREO mission concept was already anticipated in a number of pre-launch documents (Grigoryev 1993; Schmidt and Bothmer 1996; Socker et al. 1996; Davila et al. 1996a,b; Davila 1998; Socker 1998; Rust 1998; Liewer et al. 1998; Bothmer et al. 1998; Socker et al. 2000; Michels 2002; Howard et al. 2002; Davila and StCyr 2002; Mueller et al. 2003; Kaiser 2005; Harrison et al. 2005; Davis and Harrison 2005), including instrument-specific designs of the coronagraphs (Thompson et al. 2003), the EUV imager (Wülser et al. 2004), the heliospheric imager (Defise et al. 2001a,b,c; 2003; Harrison et al. 2005; Davis and Harrison 2005), the in-situ particle detectors (Luhmann et al. 2005; Blush et al. 2005), and the radio instruments (Cecconi and Zarka 2005; Rucker et al. 2005; Macher et al. 2007).

Each of the two identical STEREO spacecraft contains a set of four instrument packages (Table 1.2): (i) the *Sun Earth Connection Coronal and Heliospheric Investigation (SECCHI)* suite; (ii) the *In situ Measurments of PArticles and CME Transients (IMPACT)* experiment; (iii) the *PLAsma and SupraThermal Ion Composition (PLAS-TIC)* experiment; and (iv) the *STEREO/WAVES (SWAVES)* radio antenna system.

Table 1.2: STEREO instruments (adapted from Kaiser et al. 2008).

Instrument	Acronym	Purpose
SECCHI	COR1	Coronagraph 1.4-4.0 solar radii
	COR2	Coronagraph 2-15 solar radii
	EUVI	Extreme ultraviolet imager 1.6 solar radius
	HI-1	Heliospheric imager 8-45 solar radii
	HI-2	Heliospheric imager 35-215 solar radii
IMPACT	SWEA	Solar wind electrons to 3 keV
	STE	Suprathermal electrons 2-100 keV
	SEPT	Electrons 20-400 keV; protons 60-7,000 keV
	SIT	Composition He-Fe 300-2,000 keV/nucleon
	LET	Protons, He, heavy ions to 40 MeV/nucleon
	HET	Protons, He to 100 MeV; electrons to 8 MeV
	MAG	Vector magnetic field to 65,536 nT
PLASTIC	SWS	Protons, alpha dist. functions to 100 keV
		Heavy ions to 100 keV
	WAP	Wide angle heavy ions to 100 keV
S/WAVES	HFR	Electric field 125 kHz-16 MHz
	LFR	Electric field 2.5-160 kHz
	FFR	Fixed frequency 32 or 34 MHz
	TDS	Time domain to 250 k sample/sec

Essentially, STEREO is equipped with optical and EUV imagers (SECCHI), in-situ particle detectors and magnetometers (IMPACT, PLASTIC), and radio wave detectors (SWAVES). The SECCHI suite of instuments includes two white light coronagraphs (COR1 and COR2), an extreme-ultraviolet imager (EUVI), and two heliospheric white light imagers (HI-1 and HI-2) which track CMEs out to 1 AU. The IMPACT suite of instruments measures in situ solar wind electrons, protons, heavier ions, magnetic field strenghts, and magnetic field directions. The PLASTIC instrument measures the composition of heavy ions in the ambient plasma as well as protons and alpha particles. The SWAVES instrument uses radio waves to track the location of CME-driven shocks and the 3D topology of open field lines along which particles flow, produced by solar flares. In addition, each of the 4 instrument packages produce a small real-time stream of selected data for space weather predictions used by NOAA.

Technical descriptions of the STEREO instruments are mostly documented in the special issue of *Space Science Reviews* volume **136** (2008), which includes a description of the STEREO spacecraft (Driesman et al. 2008), the SECCHI instrument suite (Howard et al. 2008), the IMPACT instrument suite (Luhmann et al. 2008; Ullrich et al. 2008; Acuna et al. 2008; Sauvaud et al. 2008; Lin et al. 2008; Mason et al. 2008; Mewaldt et al. 2008; Müller-Mellin et al. 2008; von Rosenvinge et al. 2008), the PLASTIC instrument (Galvin et al. 2008), the SWAVES radio instrument (Bougeret et al. 2008; Bale et al. 2008; Cecconi et al. 2008), the space weather beacon facility (Biesecker et al. 2008), the STEREO ground operation (Eichstedt et al. 2008), and the education and outreach program (Peticolas et al. 2008). Post-launch instrumental studies focused on the noise and stray light correction of EUVI images (Delouille 2008;
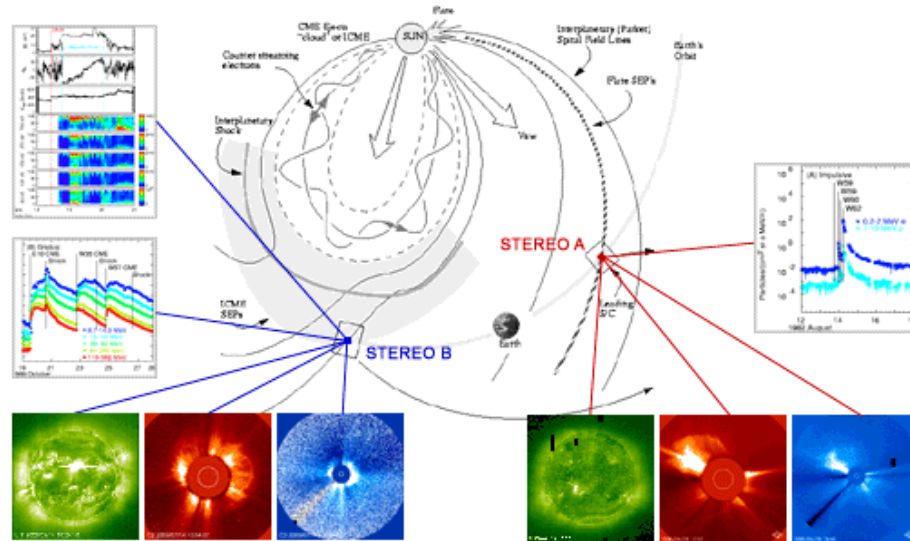
Figure 1.7: Possible STEREO/IMPACT observations of SEPs at two magnetically disconnected locations in the heliosphere: STEREO-A is located on an open magnetic field line that is connected to the coronal flare region and will probe flare-accelerated particles, while STEREO-B probes SEPs in-situ in a CME-driven shock in interplanetary space at 1 AU (Credit: IMPACT website).

Shearer et al. 2012), photometric calibration and background subtraction of the coronagraphs COR1 and COR2 (Thompson and Reginald 2008; Thompson 2010; Thompson et al. 2011; Frazin et al. 2012), the performance, calibration, and stray light rejection of the heliospheric imagers HI-1 and HI-2 (Eyles et al. 2009; Brown et al. 2009; Harrison et al. 2009; Bewsher et al. 2010, 2012; Halain et al. 2011), the antenna calibration of SWAVES (Zaslavsky et al. 2011; Oswald et al. 2009), the STEREO solar array design (Tanzman 2008), imaging software with the FITS world coordinate system (Thompson 2006; Thompson and Wei 2010), tomography software (Barbey et al. 2011), and multiscale visualization tools (Auchere et al. 2008).

The main purpose of the STEREO mission is to understand the causes and mechanisms of coronal mass ejection (CME) initiation and to follow the propagation of CMEs through the inner heliosphere to Earth (Kaiser et al. 2008). STEREO measurements are used to study the mechanisms and sites of energetic particle acceleration and to develop three-dimensional (3D) time-dependent models of the magnetic topology, temperature, density, and velocity of the solar wind between the Sun and Earth. A conceptual cartoon of the STEREO observing strategy is shown in Fig. 1.7, involving both remote-sensing and in-situ observations of a CME. The principal mission objectives of the STEREO mission is to understand the origin and consequences of CMEs, the most energetic eruptions on the Sun and the causes of the most severe nonrecurrent geomagnetic storms at Earth (Kaiser et al. 2008). The specific tasks are:

1. Understand the causes of mechanisms of CME initiation.

2. Characterize the propagation of CMEs through the heliosphere.

3. Discover the mechanisms and sites of solar energetic particle acceleration in the low corona and the interplanetary medium.

4. Develop a three-dimensional, time-dependent model of the magnetic topology, temperature, density and velocity structure of the ambient solar wind.

The scientific harvest of the STEREO mission clearly surpasses the modest expectations of the pre-launch formulated science goals, which is evident from the over 600 peer-reviewed STEREO-related publications with at least 8000 citations during the first 6 years of the mission (2007-2012). In order to give a flavor of STEREO-related scientific results and discoveries we select 10 key items that featured the highest citation rates (according to ADS in January 2013):

1. Testing the Coronal Magnetic Field Modeling: Modeling of the coronal magnetic field with *nonlinear force-free field (NLFFF)* models and quantitative comparisons with stereoscopically triangulated loops has led to a critical assessment of modeling problems, such as insufficient area coverage of vector magnetic field data that are needed to constrain the electric currents, uncertainties in the boundary data, and the non-force-freeness of the photosphere and chromosphere (DeRosa et al. 2009; Sandman et al. 2009).

2. Flux Rope Forward Modelling of CMEs: Stereoscopic observations of 26 CMEs were successfully modeled with a geometric model of a conical flux rope, which allows to determine the 3D direction of propagation, the 3D velocity and acceleration of the CME front, and the flux rope orientation and length (Thernisien et al. 2009)

3. Kinematics and Dynamics of Global Coronal EUV Waves: The kinematics of the coronal EUV wave is slower than the leading edge of the CME and decelerates, suggesting a wave initiation by the CME expanding flanks (Veronig et al. 2008), consistent with an impulsively generated fast-mode magnetoacoustic wave (Long et al. 2008; Patsourakos et al. 2009). Numerical simulations of EUV waves suggest that both MHD wave and non-wave models are required (Cohen et al. 2009), especially as evident for events observed with STEREO in quadrature (Patsourakos and Vourlidas 2009; Kienreich et al. 2009), which can even manifest a dome-shaped wave front (Veronig et al. 2010).

4. First imaging of Corotating Interaction Regions (CIR): First imaging of CIR was accomplished with the HI cameras, revealing the formation of a CIR where the fast solar wind from the equatorial coronal hole is interacting with the slow solar wind from the streamer belt (Rouillard et al. 2008).

5. Heliospheric Images of the Solar Wind and CMEs at Earth: A succession of solar wind wave fronts sweeping past Earth were observed with the HI-2 cameras from distance, synchronized with the Earth-detected arrival of density enhancements at the leading edges of high-speed solar wind streams (Sheeley et

al. 2008). Synoptic views of Earth-directed CMEs (Harrison et al. 2008), Earth-impacting CMEs (Davis et al. 2009), or other solar transients propagating to 1 AU can be tracked with HI time-elongation plots (Davies et al. 2009).

6. First Stereoscopic Triangulation of Coronal Loops: Coronal loops were stereoscopically triangulated for the first time when the spacecraft separation angle was a few degrees (Feng et al. 2007; Aschwanden et al. 2008a), which provided 3D constraints for magnetic modeling and independent density and temperature diagnostics, measured with two identical spacecraft from independent viewpoints (Aschwanden et al. 2008b).

7. Initiation of Polar Coronal Jets: Stereoscopic triangulation of a polar coronal jet reveals the helical untwisting during the initiation phase (Patsourakos et al. 2008).

8. Synchronized CME acceleration and particle acceleration: Simultaneous observations with STEREO and RHESSI reveal a synchronized evolution of the CME acceleration profile in altitude and the evolution of the hard X-ray flux or acceleration of nonthermal particles, which can be explained with the standard flare/CME magnetic reconnection flare model (Temmer et al. 2010).

9. Relation between Radio Type II Bursts and CMEs: The average height of CMEs when radio type II bursts start is found at ≈ 1.5 solar radii, corroborating the cospatial relationship between CME shocks and type II bursts (Gopalsmwamy et al. 2009).

10. First Stereoscopic Triangulation of Erupting Filaments: The first 3D triangulation of an erupting filament using EUVI followed the evolution of the eruption from 12 hours before to about 2 hours after the eruption, driven by a pre-eruptive heating phase and subsequent magnetic reconnection (Liewer et al. 2009).

Other topics of STEREO research, besides the 10 hightlights listed above, include: magnetically confined (non-eruptive), eruptive, and occulted flares (Aschwanden et al. 2009), coronal loop (MHD fast-mode) oscillations (Verwichte et al. 2009; Aschwanden 2009), acoustic (MHD slow-mode) waves (Marsh et al. 2009), 3D reconstruction of active regions (Rodriguez et al. 2009), coronal tomography and cavities (Vasquez et al. 2009; Kramar et al. 2009), solar far-side observations (Liewer et al. 2012), coronal hole super-radial expansion (Krista and Gallagher 2009), coronal-to-interplanetary radio type III mapping (Pick et al. 2009; Reiner et al. 2009; Thejappa and MacDowall 2010), 3D kinematics and tracking of CMEs in interplanetary space (Boursier et al. 2009; Maloney et al. 2009; Webb et al. 2009), solar wind sources (Luhmann et al. 2009), solar wind tomography in the heliosphere (Bisi et al. 2009), solar wind reconnection exhausts (Lavraud et al. 2009), the heliospheric current sheet (Foullon et al. 2009), *solar energetic particle (SEP)* events (von Rosenvinge et al. 2009), heliospheric transport of neutron-decay protons (Chollet and Mewaldt 2012), neutral atom imaging of a substorm (Wang et al. 2010), interplanetary dust and nanoparticles (Meyer-Vernet et al. 2009), spacecraft debris (St.Cyr et al. 2009), interstellar dust (Belheouane et al. 2012), very large amplitude whistler-mode waves in the Earth radiation

belt (Catell et al. 2008), auroral kilometric radiation (Panchenko et al. 2009), Jovian decametric emission (Panchenko et al. 2010), comet tails (Fulle et al. 2007), sun-grazing comets (Thompson 2009), search of stars with exoplanets (Wraight et al. 2011; Sangaralingam and Stevens 2011), magnetically peculiar stars (Wraight et al. 2012), and tests of black hole theories using STEREO (Valtonen et al. 2011).

Many scientific results of the STEREO mission are published in three Special issues of the journal *Solar Physics*, namely in the volumes **256**, **259** (2009), and **281** (2012), and in the *Journal of Atmospheric and Solar-Terrestrial Physics* volume **73** (2011). Reviews on STEREO-specific science can be found on theoretical modeling (Aschwanden et al. 2008; Jacobs and Poedts 2011), stereoscopy and tomography (Wiegelmann et al. 2009; Aschwanden 2011), 3D reconstruction of active regions (Aschwanden and Wülser 2011), EUV global waves (Zhukov 2011; Patsourakos and Vourlidas 2012), 3D reconstruction of prominences (Bemporad 2011), 3D reconstruction of CMEs and ICMEs (Thernisien et al. 2011; Rouillard 2011; Kleimann 2012; Howard and Tappin 2009a,b; Tappin and Howard 2009), CME observations (Webb and Howard 2012), and 3D tomography of heliospheric structures (Jackson et al. 2011).

1.4   The Hinode Mission

The Japanese/US/UK *Hinode*[6] mission (named after the Japanese word for "sunrise"), formerly known as *Solar-B*, was launched on 2006 September 22, just a month before the STEREO mission. The satellite was maneuvered into a quasi-circular Sun-synchroneous orbit that is geostationary over the Earth day/night terminator, which allows near-continuous observation of the Sun. The first images from Hinode were captured on 2006 October 28. The Hinode satellite contains three telescopes; (i) the *Solar Optical Telescope (SOT)*; (ii) the *X-ray telescope (XRT)*; and (iii) the *Extreme-Ultraviolet Imaging Spectrometer (EIS)*, pictured in Fig. 1.8 and technical data are listed in Table 1.3.

The SOT (Solar Optical Telescope) is a Gregorian type with 0.5 meter aperture and with an angular resolution of $\approx 0.2''$ over a limited field-of-view of $\approx 400'' \times 400''$. The *Focal Plane Package (FPP)* consists of three optical instruments: the *Broadband Filter Imager (BFI)* which produces images of the solar photosphere and chromosphere in 6 wide-band interference filters; the *Narrowband Filter Imager (NFI)* which is a tunable Lyot-type birefringent filter capable of producing magnetogram and dopplergram images of the solar surface; and the *Spectropolarimeter (SP)* which produces the most sensitive vector magnetograph maps of the photosphere to date. The FPP also includes a *Correlation Tracker (CT)* which locks onto solar granulation to stabilize the SOT iamges to a fraction of an arcsecond. The spatial resolution of the SOT is about 5 times finer than MDI/SOHO.

The XRT (X-Ray Telescope) is a modified Wolter 1 type telescope design that uses grazing incidence optics to image the solar corona's hottest components (with temperatures of $T_e \approx 0.5 - 10$ MK) with an angular resolution that is about twice the CCD pixel size of $1''$, over an imaging field-of-view of 34 arcminutes, which is slightly
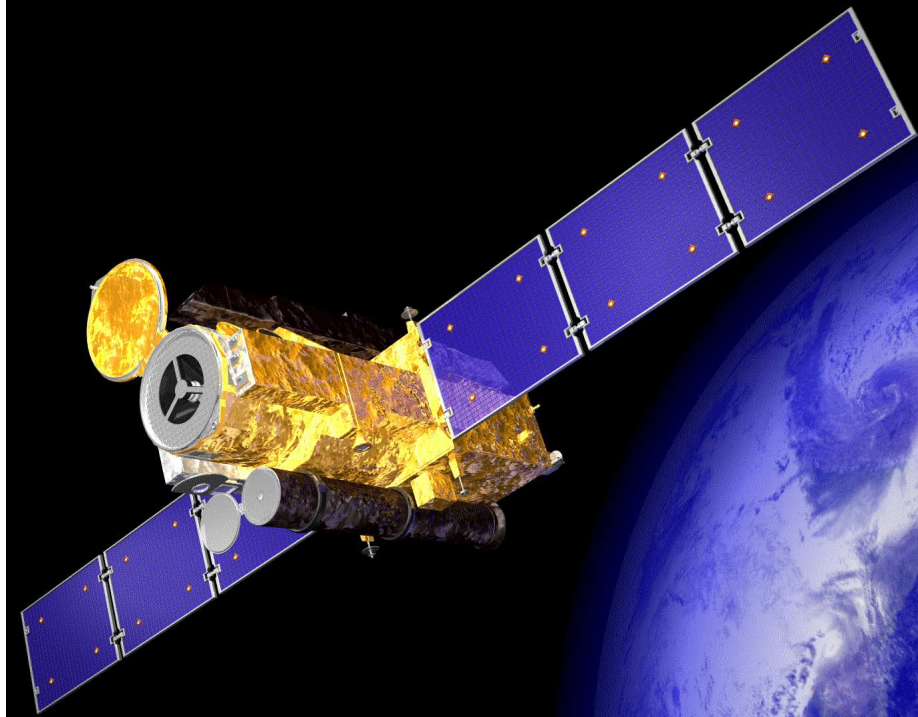
---

[6]http://hinode.msfc.nasa.gov/

Figure 1.8: Artist's version of the *Hinode* spacecraft in a Sun-synchroneous orbit. The large central cyclinder with the open door is the SOT telescope, while the EIS instrument is in the black box on top, and the XRT instrument is attached below the SOT (Courtesy of Hinode Team).

larger than the solar diameter, so that it is capable to capture a full-Sun image when pointed at Sun center.

The EIS (Extreme-Ultraviolet Imaging Spectrometer) is a normal incidence spectrometer in the extreme ultraviolet (EUV) wavelength range, producing spatially resolved spectra in the two wavelength ranges of 17.0-21.2 nm (170-212 Å) and 24.6-29.2 nm (246-292 Å). The spatial resolution is $\approx 2''$ and the field-of-view is up to $560'' \times 512''$. The emission lines in the EIS wavelength bands are emitted at coronal temperatures ranging from 50,000 K to 20 MK.

Technical descriptions of the Hinode instruments are given in the special issues of *Solar Physics* volume **243** (2007) and **249** (2008), containing descriptions of the mission (Kosugi et al. 2007), the data archive (Matsuzaki et al. 2007), the XRT instrument (Golub et al. 2007; Kano et al. 2007), the EIS instrument (Culhane et al. 2007), and the SOT instrument (Tsuneta et al. 2008; Shimizu et al. 2008; Suematsu et al. 2008; Ichimoto et al. 2008). Post-launch instrumental studies of Hinode focused on the point spread function of SOT (Wedemeyer-Boehm 2008), the response function of SOT (Wachter 2008), image processing techniques applied to SOT (Tavabi et al. 2012), magnetogram comparisons of SOT (Wang et al. 2009), polarimetric noise and scat-

Table 1.3: Hinode Instrument Characteristics (adapted from Kosugi et al. 2007).

Parameter	Characteristics
Spacecraft mass:	900 kg (wet), 770 kg (dry)
Spacecraft power:	1100 W
Spacecraft size:	$4.0 \times 1.6 \times 1.6$ m
Data rate:	up to 2 Mbps
Telemetry rate:	32 kbps (S-band), 4 Mbps (X-band)
On-board storage:	8 Gbits
Orbit altitude:	680 km (circular, Sun-synchronous, polar orbit)
Orbit inclination:	$98.1°$
Orbit period:	98 min
Attitude control:	three-axis stabilized
Absolute pointing:	$20''$
Pointing determination:	X/Y axes: $0.1''$
Launch date:	2006 September 22
Instruments:	Solar Optical Telescope (SOT)
	X-ray telescope (XRT)
	Extreme-Ultraviolet Imaging Spectrometer (EIS)
Angular resolution:	SOT: $0.2''$, XRT: $2''$, EIS: $2''$
Field of view:	SOT: $400''$, XRT: 34', EIS: $\leq 560''$
Temporal resolution:	SOT: 3.4 s, XRT: 2 s, EIS: scanning $1''$ in 0.7 s
Spectral range:	SOT: 3800-7000 Å, EIS: 170-212 Å, 246-292 Å, XRT: 6-60 Å

tering polarization of SOT (Tiwari et al. 2009; Snik et al. 2010), spectro-polarimetric inversion of Stokes profiles (Borrero et al. 2011; VanNoort 2012), the intensity contrast and stray light correction of SOT (Danilovic et al. 2008; Mathew et al. 2009), transverse flow measurements with optical flow techniques (Chae et al. 2008, 2009), Fabry-Perot versus slit spectro-polarimetry analysis (Judge et al. 2010), speckle interferometry comparisons with SOT (Woeger et al. 2008), the wavelength calibration of EIS (Brown et al. 2007, 2008; Landi and Young 2010; Wang et al. 2011), on-orbit sensitivity monitoring of EIS (Mariska 2012), and the Hinode solar flare catalog (Watanabe et al. 2012).

As the successor of the *Yohkoh* (Solar-A) mission, Hinode aims to understand how magnetic energy gets transferred from the photosphere to the upper atmosphere and results in explosive energy releases. The principal scientific goals of the Hinode mission are the following (Kosugi et al. 2007):

1. To understand the processes of magnetic field generation and transport including the magnetic modulation of the Sun's luminosity.

2. To investigate the processes responsible for energy transfer from the photosphere to the corona and for the heating and structuring of the chromosphere and the corona.

3. To determine the mechanisms responsible for eruptive phenomena, such as flares and coronal mass ejections, and understand these phenomena in the context of

the space weather of the Sun-Earth system.

Hinode is designed to address the fundamental question of how magnetic fields interact with the ionized atmosphere to produce solar variability, which should be accomplished by the unprecedented high spatial resolution of Hinode (see examples in Fig. 1.9) to measure magnetic fields from space, which is only diffraction-limited, compared with ground-based optical telescopes that suffer degraded spatial resultion due to the seeing conditions in the Earth's atmosphere. The three instruments were selected to observe the response of the chromosphere and corona to changes in the photosphere by measuring the 3D vector magnetic field. This should constrain the measurement of electric currents and free magnetic energies (defined as difference between the force-free non-potential and potential field). The response of the solar atmosphere to magnetic field changes is measured by the EUV Imaging Spectrometer (EIS) and the X-Ray Telescope (XRT).

Reviewing the scientific output of the Hinode mission, which totals to over 750 peer-reviewed publications with 13,000 citations during the first 6 years of the mission (2007-2012), we select 10 highlights and/or discoveries that featured the highest citation rates (according to ADS in January 2013):

1. Chromospheric Alfvénic Waves Powering the Solar Wind: The signature of ubiquitous Alfvén waves have been detected in the chromosphere with SOT, manifested as quasi-periodic jet-like extrusions called spicules, with amplitudes of 10-25 km s^{-1} and periods of 100-500 s, carrying sufficient flux to accelerate the solar wind and possibly to heat the quiet corona (DePontieu et al. 2007a). Spicules are believed to appear in two forms: shock-driven type I spicules, and more dynamically and rapidly heated type II spicules (DePontieu et al. 2007b). Type II spicular jets may even contribute to coronal heating (DePontieu et al. 2009, 2011).

2. Horizontal Magnetic Fields of the Quiet-Sun Internetwork: SOT/SP measurements of the 3D vector magnetic field in the quiet Sun revealed that the internetwork regions are permeated by relatively strong horizontal magnetic flux, with an average horizontal flux density of $B_{\parallel} = 55$ Mx cm^{-2}, as compared to the corresponding average vertical flux density of $B_{\perp} = 11$ Mx cm^{-2}, probably organized by magneto-convection on meso-granular scales (Lites et al. 2008). Emergence of small-scale ($\lesssim 2''$) magnetic flux was detected with SOT/SP in the quiet-Sun internetwork also (Centeno et al. 2007). The internetwork has highly inclined fields of $B \approx 100 - 800$ G, while the network areas have field strengths of $B \approx 1 - 2$ kG (Orozco Suarez et al. 2007).

3. Evidence for Alfvén Waves in Solar X-Ray Jets: Hinode/XRT observations of polar coronal holes revealed that soft X-ray jets have two distinctly different velocities, one near the Alfvén speed ($v_A \approx 800$ km s^{-1}), and one near the sound speed ($c_s \approx 200$ km s^{-1}), which may contribute to the high-speed solar wind (Cirtain et al. 2007).
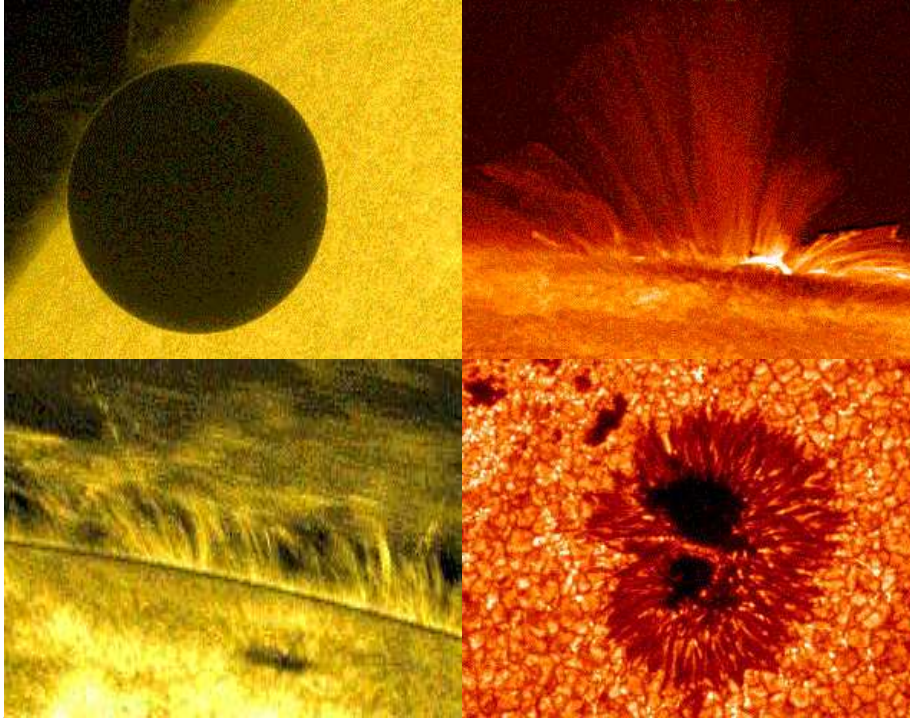
Figure 1.9: Images obtained from Hinode that emphasize the high spatial resolution of SOT that is needed to resolve the finest observed features. *Top left:* Venus transit on 2012 June 5; *Bottom left:* Prominence threads above the limb; *Top right:* Postflare loops; *Bottom right:* Sunspot and solar granulation (Courtesy of Hinode Team).

4. Transverse MHD Waves in Prominences: Hinode/SOT observations of fine-scale thread-like structures in prominences reveal oscillations with periods of several minutes, likely to be caused by MHD fast-mode Alfvén waves (Okamoto et al. 2007).

5. Non-Linear Force-Free Magnetic Field (NLFFF) Modeling of Solar Flares: was conducted with Hinode/SOT vector magnetic field data and 14 NLFFF codes, revealing strong electrical currents that emerge together with the magnetic flux before a flare in a large-scale twisted flux rope topology, liberating a free magnetic energy of $\approx 10^{32}$ erg during an X3.4 GOES-class flare (Schrijver et al. 2008).

6. Quiet-Sun EUV Emission Lines and Diagnostics: The EUV spectrum of the Quiet Sun comprises many emission lines from iron (Fe VIII to XXIV), oxygen (O IV to O VI), magnesium (Mg V to Mg VII), silicon (Si VII to X) and others, which enables unprecedented temperature and density diagnostics with the Hinode/EIS spectrometer (Young et al. 2007; 2009).

7. Chromospheric Anemone Jets as Evidence of Ubiquitous Reconnection: Hinode

SOT observations of jets outside sunspots in active regions with lengths of $3''$-$7''$, widths of $0.2''$-$0.4''$, and velocities of 10-20 km s^{-1} reveal inverted-Y geometries that are indicative of ubiquitous small-scale magnetic reconnection (Shibata et al. 2007).

8. Quiescent Prominence Dynamics: Hinode/SOT observed upflows with sonic speeds of ≈ 10 km s^{-1}, filamentary downflows, turbulent vortices, and large-scale transverse oscillations with periods of 20-40 min and amplitudes of 2-5 Mm in quiescent prominences, all dynamic phenomena that are thermally and/or magnetically driven (Berger et al. 2008).

9. Continuous Plasma Outflows as Sources of Solar Wind: A possible origin of the fast solar wind has been identified with Hinode/XRT at the edge of active regions, where continuous outflows of soft X-ray emitting plasma along open magnetic field lines was observed, with a total mass loss rate of $\approx 1/4$ of the solar wind (Sakao et al. 2007).

10. Solar Surface Emerging Flux Regions have been modeled with 3D radiative MHD simulations originating from the rise of buoyant magnetic flux tubes through the convection zone into the photosphere, which can explain the features observed with Hinode/SOT, such as the pattern of emerging flux regions, magnetic flux cancellation, associated high-speed downflows, convective collapse of photospheric flux tubes, appearance of anomalous darkenings, formation of bright points, and $B \approx 1$ kG horizontal magnetic fields (Cheung et al. 2008).

Some initial scientific results from *Hinode* are documented in the special issue of *Science* volume **318** (2007), while ongoing Hinode research is well captured in the conference series of the *Astronomical Society of the Pacific*, such as from the 2nd Hinode Science Meeting (ASP volume **415**, 2009), the 3rd Hinode Science Meeting (ASP volume **454**, 2012), the 4th Hinode Science Meeting (ASP volume **455**, 2012), and the 5th Hinode Science Meeting (ASP volume **456**, 2012). An online source of new Hinode/EIS scientific findings is the *Hinode/EIS Nuggets Archive*[7]. Some partial reviews of Hinode-specific science results can be found in Harra (2008), Sekii (2009), McKenzie (2009), Suematsu (2010), Tsuneta (2011), and Patsourakos and Vourlidas (2012).

1.5   The SDO Mission

The *Solar Dynamics Observatory (SDO)*[8] is the first space-based mission of NASA's *Living With a Star* program. SDO was launched on 2010 February 11 and lifted into a circular geosynchroneous orbit inclined by $28°$ about the longitude of the SDO-dedicated ground station in New Mexico (Fig 1.10). Science operations started on 2010 May 1. The SDO spacecraft contains three instruments, the *Atmospheric Imaging Assembly (AIA)*, the *Extreme Ultraviolet Variability Experiment (EVE)*, and the

---

[7]http://msslxr.mssl.ucl.ac.uk:8080/SolarB/eisnuggets.jsp
[8]http://www.nasa.gov/mission_pages/sdo/main/index.html

Figure 1.10: The *Solar Dynamics Observatory (SDO)* spacecraft is shown in an artist's impression. The four golden tubes represent the four *Atmospheric Imaging Assembly (AIA)* telescopes (Courtesy NASA and SDO Team).

Helioseismic and Magnetic Imager (HMI), built by NASA/GSFC, LMSAL, and LASP (University of Colorado). Technical data of the SDO spacecraft (Fig. 1.10) are summarized in Table 1.4.

The AIA (Atmospheric Imaging Assembly) consists of four telescopes that employ normal-incidence, multilayer-coated optics to provide narrow-band imaging of seven extreme ultra-violet (EUV) band passes centered mostly on iron lines: Fe XVIII (94 Å), Fe VIII and XXI (131 Å), Fe IX (171 Å), Fe XII and XXIV (193 Å), Fe XIV (211 Å), He II (304 Å), and Fe XVI (335 Å). One telescope observes C IV (near 1600 Å) and the nearby continuum (1700 Å) and has a filter that observes in the visible to enable coalignment with images from the other telescopes. The temperature diagnostics of the EUV emissions cover the range from $T_e = 6 \times 10^4$ K to $T_e = 20$ MK. The field-of-view of AIA images extends out to 1.5 solar radii, the CCD image contains 4096×4096 pixels with a pixel size of $0.6''$ and has a spatial resolution of ≈ 2 pixels. Images in all wavelengths are recorded with a cadence of 12 s, 24 hours a day, producing over a Terabyte of (uncompressed) data per day. Examples of coronal loops, filaments, and prominences imaged by AIA are shown in Fig. 1.11.

The EVE (Extreme Ultraviolet Variability Experiment) measures the solar EUV irradiance from 0.1 to 105 nm (1-1050 Å) with unprecedented spectral resolution (0.1 nm), temporal cadence (10 s), and accuracy (20%). EVE includes several irradiance instruments: The *Multiple EUV Grating Spectrographs (MEGS-A)* is a grazing-incidence spectrograph that measures the solar EUV irradiance in the 5-37 nm range

wit 0.1-nm resolution, and the MEGS-B is a normal-incidence, dual-pass spectrograph that measures the solar EUV irradiance in the 35-105 nm range with 0.1-nm resolution. In-flight calibration is provided by the *EUV Spectro-Photometer (ESP)*, which measures the solar EUV irradiance in broadbands between 0.1 and 39 nm. All these instruments are designed to accurately measure the solar irradiance in the entire EUV wavelength range and its impact on the Earth's ionosphere.

The HMI (Helioseismic and Magnetic Imager) onboard SDO is a vector magnetograph that is designed to measure the Doppler shift, inensity, and vector magnetic field at the solar photosphere using the 6173 Å Fe I absorption line. The instrument consists of a front-window filter, a telescope, a set of waveplates for polarimetry, an image stabilization system, a blocking filter, a five-stage Lyot filter with one tunable element, two wide-field tunable Michelson interferometers, a pair of 4096^2 pixel CCD cameras with independent shutters, and associatd electronics. Each camera takes a full-disk image in Doppler velocity, intensity, and line-of-sight field measurements with a cadence of 45 s, and a slower cadence for a full vector magnetic field.

Technical descriptions of the SDO instruments are mostly given in the special issue of *Solar Physics* volume **275** (2012), such as descriptions of the SDO mission (Pesnell et al. 2012), the AIA instrument (Lemen et al. 2012; Boerner et al. 2012; Golub 2007), the EVE instrument (Woods et al. 2012; Hock et al. 2012), the HMI instrument (Scherrer et al. 2012; Schou et al. 2012a,b; Wachter et al. 2012), Couvidat et al. 2012a, 2012b; Zhao et al. 2012), the solar event catalogization, called *Heliophysics Event Knowledgebase (HEK)* (Hurlburt et al. 2012), the automated feature detection algorithms (Martens et al. 2012), the education and outreach program (Drobnes et al. 2012), a German-based SDO center (Burton et al. 2008), or the *Virtual Solar Observatory (SVO)* facility (Hill et al. 2009). Post-launch instrumental SDO studies concerned the SDO/AIA response function (O'Dwyer et al. 2010), fast inversion of Stokes Vector profiles (Borrero et al. 2011), inter-comparisons of magnetograms (Liu et al. 2012a,b; Pietarila et al. 2013), and intercomparisons of AIA and HMI images (Chandrashekhar et al. 2012).

The science goals of solar-dedicated missions have been increasingly broadened over the past, embracing now a fundamental understanding of the physics of solar variations as well as its consequences on the Sun-Earth system and heliosphere. The official SDO level 1 science requirements were formulated in form of seven questions (Pesnell et al. 2012):

1. What mechanisms drive the quasi-periodic 11-year cycle of solar activity?

2. How is active region magnetic flux synthesized, concentrated, and dispersed across the solar surface?

3. How does magnetic reconnection on small scales reorganize the large-scale field topology and current systems, and how significant is it in heating the corona and accelerating the solar wind?

4. Where do the observed variations in the Sun's extreme ultraviolet spectral irradiance arise, and how do they relate to the magnetic activity cycles?

Table 1.4: SDO Instrument Characteristics.

Parameter	Characteristics		
Spacecraft mass:	3000 kg		
Spacecraft power:	1500 W		
Spacecraft size:	$4.7 \times 2.2 \times 2.2$ m		
Data rate:	150 Mbps		
Orbit altitude:	35,800 km		
Orbit inclination:	$28°$		
Orbit period:	geosynchronous		
Attitude control:	three-axis stabilited		
Pointing accuracy:	$0.12''$		
Launch date:	2010 February 11		
Misson Operation:	NASA/GSFC		
SDO Ground Station:	White Sands, New Mexico		
Instrument:	AIA	HMI	EVE
CCD detector:	4096×4096	4096×4096	1024×2048
Pixel size:	$0.6''$	$0.505''$	
Angular resolution:	$1.5''$	$0.91''$	
Field of view:	$41' \times 41'$	$34' \times 34'$	
Temporal cadence:	12 s	45 s	10 s
Spectral range:	94 Å (Fe XVIII)	6173 Å	1-1050 Å
	131 Å (Fe VIII,XXI)		
	171 Å (Fe IX)		
	193 Å (Fe XII,XXIV)		
	211 Å (Fe XIV)		
	304 Å (He II)		
	335 Å (He XVI)		
	1600 Å (C IV+cont)		
	1700 Å (cont)		
	4500 Å (cont)		

5. What magnetic field configuration lead to the coronal mass ejections, filament eruptions, and flares that produce energetic particles and radiation?

6. Can the structure and dynamics of the solar wind near Earth be determined from the magnetic field configuration and atmospheric structure near the solar surface?

7. When will activity occur, and is it possible to make accurate and reliable forecasts of space weather and climate?

These science questions then led to the design of the SDO instruments. All of the questions are related to developing a fundamental understanding of the solar magnetic field. Three of the science questions emphasize predicting solar activity.

At the time of writing, SDO completed the third year of its mission and produced already some 300 peer-reviewed publications with over 2000 citations. In order to give a flavor of the scientific discoveries and new observational results we select the 10 most-cited topics (according to ADS in January 2013):
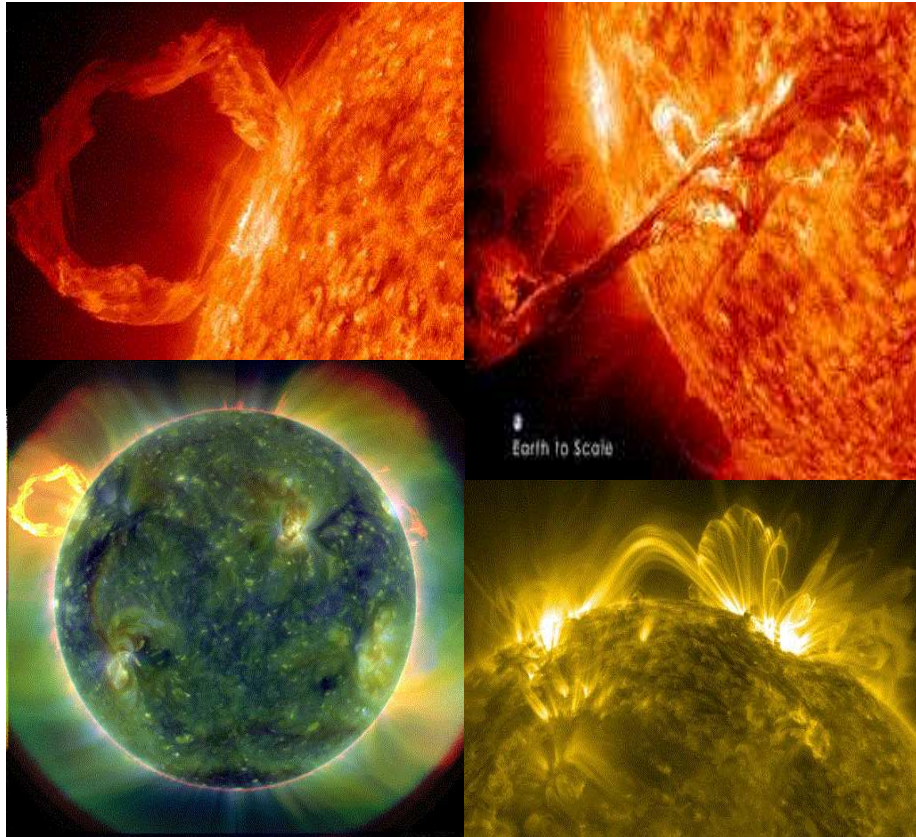
Figure 1.11: Images taken by AIA/SDO. *Top left:* Prominence observed with AIA in 304 Å on 2012 August 31; *Bottom left:* Full disk EUV multi-wavelength image on 2012 August 31; *Top right:* An erupting filament that turns into a prominence; *Bottom right:* Two active regions near the limb bridged by transequatorial loops, observed by AIA on 2012 July 12 (Courtesy of NASA and SDO Team).

1. Quasi-Periodic Fast-Mode MHD Global EUV Waves: Quasi-periodic wave trains with Alfvénic speeds (≈ 1400 km s^{-1}) were discovered to run ahead of the lateral CME front, as well as ahead of the secondary slower EUV wave inside the CME front (Liu et al. 2012). A similar fast-mode wave preceding the slower EUV wave was discovered earlier with AIA (Chen and Wu 2011).

2. Iso-thermal Cross-sections of Active Region Loops: have been inferred from differential emission measure (DEM) analysis of background-subtracted loop cross-sections, using the full temperature range of AIA. This result is in contrast to the multi-thermal nature expected for coronal heating models by nanoflares (Aschwanden and Boerner 2011). Multi-stranded loop ensembles were found to be multi-thermal (Schmelz et al. 2011).

3. Long-range Magnetic Coupling Between Flares and CMEs: This study revealed near-synchronous, long-distance global coupling (over more than a solar radius) between magnetic domains that exhibit flares, eruptions, and minor forms of activity (Schrijver and Title 2011).

4. Evolution of Magnetic Field during Major Eruptive Flares: Fast magnetic flux emergence (over 5 days) and strong shearing motion led to a quadrupolar sunspot complex that produced several major eruptions, including the first X-class flare (2011 February 14) of Solar Cycle 24. Magnetic (NLFFF) modeling yields free energies of $\approx 2.6 \times 10^{32}$ erg. The flare-associated changes in the magnetic field were found to be consistent with the coronal "implosion" model (Sun et al. 2012).

5. The 2011 February 15, X2 Flare and MHD Flux-Rope Modeling: The 3D evolution of this major flare, its footpoint ribbons, coronal front, and associated CME is aided by the combined view of AIA and STEREO and is modeled with a flux-rope MHD simulation, which reproduces the (streamer-confined) lateral and adiabatic volume expansion of the CME, as well as the global EUV wave self-consistently (Schrijver et al. 2011). HMI revealed a rapid (30 min) and irreversible enhancement in the horizontal magnetic field at the flaring magnetic polarity inversion line by $\approx 30\%$ during the same flare (Wang et al. 2012) and a "sunquake" wave in response (Kosovichev 2011).

6. Heating of High-Temperature Active Region Loops: The core of active regions appears to be steadily heated to temperatures of $T_e \approx 4$ MK, so that they reach an equilibrium between heating and cooling loss rates (Warren et al. 2011). Warm loops ($T_e \approx 1$ MK) have been consistently diagnosed with SDO/AIA and Hinode/EIS (Del Zanna et al. 2011).

7. Flux-Rope Formation: The flux rope formation during the CME impulsive phase has been observed during the 2010 November 3 flare (Cheng et al. 2011), accompanied with a high-temperature erupting plasmoid (Reeves and Golub 2011).

8. Sigmoids: A transition from a sigmoid to a flux rope during a tether-cutting reconnection with subsequent eruption of a loop-like CME was disentangled during the 2010 August 1 event (Liu et al. 2010).

9. Coronal Kink-Mode Loop Oscillations: This first AIA detection of kink-mode loop oscillations revealed vertical oscillations in the loop plane (with periods of ≈ 6.3 min), coupled cross-sectional and density oscillations, no damping of the oscillation amplitude, multi-strand oscillations with slightly ($\approx 10\%$) different periods, a relatively cool loop temperature ($T_e \approx 0.5$ MK), and a magnetic field of $B \approx 4$ G (Aschwanden and Schrijver 2011).

10. CME Shock Wave: A particularly well-observed shock ahead of a bubble-like CME was found to have a density compression of 1.56, a temperature of 2.8 MK, a thickness of ≈ 20 Mm, a speed of 600 km s^{-1} decreasing to 550 km s^{-1}, and a lateral expansion speed of 400 km s^{-1} (Ma et al. 2011).

Figure 1.12: Artist's view of the CORONAS-Photon spacecraft in orbit (image credit: Roskosmos).

The content of the foregoing selection of SDO publications demonstrates the preponderance and special aptitude of SDO observations to disentangle the dynamics of flares, coronal mass ejections, associated shock waves, magnetoacoustic waves, global EUV waves, EUV dimming, sunquakes, active region loops, sigmoids, flux ropes, jets, polar crowns, filaments, and prominences. Many studies are focused on the role of the magnetic field and the associated Lorentz and hydrodynamic forces, which drive magnetic and fluid instabilities (e.g., kink instability, torus instability, Kelvin-Helmholtz instability, Rayleigh-Taylor instability), lead to a loss of equilibrium and to eruptive magneto-hydrodynamic evolutions. Additional topics of SDO studies are coronal heating, nanoflare scenarios, spicular heating, solar cycle variations, local helioseismology diagnostics, far-side helioseismology, magnetic flux emergence, subsurface flows, coronal magnetic field modeling, space weather forecasting, helio-climatology, as well as Sun-grazing comets, and a Venus transit (Fig. 1.9).

1.6   The CORONAS Missions

The *Russian Federal Space Agency* (Roskosmos) launched a series of three solar-terrestrial science missions: *CORONAS-I* was launched on 1994 March 2 and decayed on 2001 March 4 (I stands for Izmiran, the site of the head institution, the *Institute of Terrestrial Magnetism, Ionosphere and Radio Wave Propagation*); *CORONAS-F* was launched on 2001 July 31 and re-entered the atmosphere on 2005 December 6 (F stands for FIAN, the Lebedev Institute of Physics); and *CORONAS-Photon* (or CORONAS-

Foton), which was launched on 2009 January 30, but lost power on 2009 December 1, and was declared as lost on 2010 April 18 (Fig. 1.12). The *CORONAS* project, an acronym for *Complex ORbital Observations Near-Earth of Activity of the Sun*, was envisioned to make observations during different phases of the 11-year solar cycle. The CORONAS satellite series was equipped with a variety of instruments including UV, EUV, and XUV imagers, X-ray and gamma-ray spectrometers, radio receivers, and particle counters.

CORONAS-I carried a total of 12 science instruments, including the *Terek* spectrohliometer, the *RES-K* solar X-ray spectrograph, the *Helikon* solar gamma-ray detector, the *SUVR-SP-C* ultravioet radiometer, the *DIFOS* optical photometer, and other instruments.

CORONAS-F was equipped with 18 instruments: the Multichannel Solar Photometer *DIFOS*, the Full Sun XUV spectroscopy imaging *SPIRIT* (Zhitnik et al. 2002; Reva et al. 2011), the Solar X-Ray Telescope *SRT*, the X-Ray Spectroheliograph *RES*, the X-Ray Spectrometer and Photometer *DIOGENESS* (Plocieniak et al. 2002), the X-Ray Spectrometer *RESIK*, the Solar Spectropolarimter *SPR*, the Flare Spectrometer *IRIS*, the Gamma Spectrometer *HELICON*, the X-Ray Spectrometer *RPS* (Pankov et al. 2006), the Time-Amplitude Spectrometer *AVS*, the Solar UV Radiometer *SUFR*, the Solar UV Spectrophotometer *VUSS*, the Solar Cosmic Rays Complex *SKL*, the Cosmic Ray Monitor *MKL*, the Spectrometer of Energy and Ion Chemical Composition *SKI*, the Solar Neutron and Gamma Ray Spectrometer *SONG*, and the X-ray polarimeter *PR-N*. Technical publications of the CORONAS-F instruments are mostly given in the special issue of *Solar System Research* volume **45** (2011), and additional publications summarize the studies of solar activity on the CORONAS-F satellite (Oraevsky and Sobelman 2002), or deal with radiation doses in the *International Space Station (ISS)* compared with CORONAS-F (Panasyuk et al. 2007), and the final orbits of CORONAS-F (Boldyrev et al. 2007).

CORONAS-Photon is part of the international *Living with a Star (LWS)* program. The scientific payload complex contains: the high energy spectrometer *Natalya-2M*, (Kotov et al. 2011c), the Roentgen Telescope-2 *RT-2* (Kotoch et al. 2011; Sreekumar et al. 2011; Sarkar et al. 2011; Debnath et al. 2011; Nandi et al. 2011; Rao et al. 2011), the hard X-ray polarimeter-spectrometer *PENGUIN-M* (Kotov et al. 2011a), the X-ray and gamma-ray spectrometer *Konus-RF*, the fast X-ray monitor *BRM*, (Trofimov et al. 2011), the multi-channel ultraviolet monitor *PHOKA*, (Kotov et al. 2011b), the X-ray and gamma-ray spectrometer *Konus-RF*, the solar telescope/imaging spectrometer *TESIS* (Kuzin et al. 2009, 2011a,b), which contains the *SphinX soft X-ray spectrophotometer* (Gburek et al. 2011a,b; 2013), the charged particle analyzer *Electron-M-PESCA*, (Denisov et al. 2011), the satellite telescope of electrons and protons *STEP-F* (Dudnik et al. 2011, 2012), the magnetometer *SM-8M*, and the global solar oscillation experiment *SOKOL* (Levedev et al. 2011). Scientific goals and observational capabilities of the CORONAS-Photon mission are summarized in Kotov (2010, 2011), the data processing in Alikin et al. (2011), and the ground operations in Buslov et al. (2011).

The main goal of the CORONAS project is the investigation of energy accumulation and its transformation into energy of accelerated particles processes during solar flares; the study of the acceleration mechanisms, propagation and interaction of

fast particles in the solar atmosphere; the study of the solar activity correlation with physical-chemical processes in the Earth upper atmosphere. The specific science tasks include:

1. Determine the distribution functions of accelerated electrons, protons and nuclei and their dynamics with high time resolution.

2. Study the difference in the acceleration dynamics of electrons and protons (nuclei).

3. Obtain the distribution function variations for high energy particles (up to a few GeV).

4. Study the interacting particle angular anisotropy by statistical analysis of radiation spectra and linear polarization parameters of hard X-rays.

5. Study of directional effects in the region of high energy gamma radiation.

6. Determination of mechanisms and requirements of electron and proton acceleration in different flare phases, and parameters of propagation region of accelerated particles.

7. Determination of elemental abundance in the region of gamma-ray production by gamma spectroscopy and capture of low energy neutrons in the solar atmosphere.

8. Determination of radiation generation altitudes by observation of deuteron line weakening from limb flares.

9. Determination of energy spectra in view of accelerated protons and nuclei and dynamics of these spectra according to nuclear gamma-line ratio.

10. Study of light elements generation (D, 3He, Li, Be) during flares.

11. Research of chemical and isotopic compositions of nuclei accelerated in flare on the Earth orbit, and also energy and temporal parameters of flare electrons and protons.

12. Monitoring of the Earth upper atmosphere by absorption of extreme ultraviolet of the quiet Sun.

13. Study of hard X-ray and gamma radiation from gamma-ray bursts.

14. Study of X-ray radiation from the bright local sources along the ecliptic plane.

Scientific results and instrumental descriptions of the CORONAS missons are documented in at least 75 peer-reviewed publications in English language (not counting publications in Russian) and the most-cited results include (according to ADS in January 2013):

1. Quasi-periodic pulsations in gamma-ray emission during the solar flare of 2005 January 1, detected at photon energies up to 2-6 MeV with the *SOlar Neutrons and Gamma-rays (SONG)* experiment aboard the CORONAS-F mission, as well as with RHESSI and the Nobeyama radio heliograph (Nakariakov et al. 2010).

2. The Temperature Structure of the Low-Activity Corona: (GOES-class A9-B5) shows a double-peaked *differential emission measure (DEM)* distribution (based on RESIK spectra) with a peak at $T_e \approx 2 - 3$ MK, but also a much weaker peak at hotter plasma of $T_e \approx 10$ MK (Sylwester et al. 2010a).

3. High-Temperature Diagnostics During Solar Flares: has been systemtatically observed with SPIRIT in the 280-330 Å wavelength range ($log(T_e) \approx 6.8 - 7.2$) during 2001-2005 with ten thousands of spectro-heliograms (Shestov et al. 2010). The solar X-ray continuum was also measured for 19 flares during 2002-2003 with RESIK (Phillips et al. 2010a), and a DEM inversion algorithm has been tested with SPIRIT spectra (Goryaev et al. 2010).

4. Potassium, Argon, and Chlorine Abundances: Potassium lines were analyzed with RESIK at $3.53 - 3.57$ Å, revealing an enhancement of the first-ionization potential (FIP) effect by a factor of 5.5, suggesting fractionation in the lower chromosphere (Sylwester et al. 2010b). Argon lines analyzed with RESIK at $3.9 - 3.7$ Å were found to have a very similar photospheric and coronal abundance (Sylwester et al. 2010c). Chlorine abundances determined with RESIK show a enhancement of 1.8 and 2.7 compared with infrared sunspot measurements (Sylwester et al. 2011).

5. High-Energy Gamma Radiation of Solar Flares: was detected with SONG up to energies of > 100 MeV, suggesting decay of neutral pions by > 300 MeV protons, during the 2001 August 25, X5.3 flare (Kurt et al. 2010a,b), and during the 2003 October 28, X17.2 flare (Kuznetsov et al. 2011).

A summary of scientific results from the CORONAS-F mission is given in Kuznetsov et al. (2011).

1.7 Other Solar Space and Suborbital Missions

In addition to the large space-based and solar-dedicated observatories[9], (e.g., SOHO, STEREO, Hinode, SDO) that are operational at the beginning of the 21st century, there is in also an arsenal of other (mostly smaller, or partially solar-dedicated) space missions, suborbital rocket flights, and balloon-borne detectors, that provided significant contributions to solar physics. In the following we will briefly mention a few of these missions that are operational at the beginning of the 21st century, in order of launch dates.

The *Geostationary Operational Environmental Satellites (GOES)* (Fig. 1.13) program, operated by the US *National Oceanic and Atmospheric Administration (NOAA)*,

---

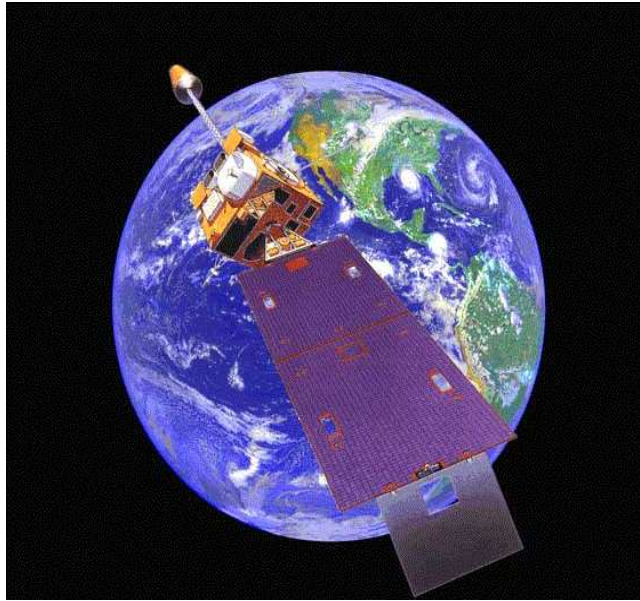[9]http://www.scholarpedia.org/article/Solar_Satellites

Figure 1.13: The Geostationary Operational Environmental Satellite (GOES-10), which was deactivated on 2009 December 2, after 12 years of service (Credit: NOAA).

consists of a series of geostationary satellites (orbiting the Earth at a height of 35,790 km), which overlap in time so that there are always one to three spacecraft present and guarantee an essentially uninterrupted time series of solar soft X-ray fluxes, besides continuous meteorological observations of the Earth. The GOES-1 satellite was launched on 1974 October 16, and GOES-2 and GOES-3 followed in 1977 and 1978. In the meantime the series continued up to GOES-15, launched on 2010 March 4, while the future satellites GOES-R and GOES-S (with soft X-ray imaging capabilities) are in the queue for a launch in 2015 and 2017, respectively. Operational and technical details of GOES satellites can be gleaned from Grubb (1975), Donnelly et al. (1977), Bouwer et al. (1982), Thomas et al. (1985), Kahler and Kreplin (1991), Garcia (1994), Shing et al. (1999), Lemen et al. (2004), Stern et al. (2004), Hill et al. (2005), Pizzo et al. (2005), White et al. (2005), Väänänen et al. (2009), Evans et al. (2010), Neupert (2011), the NOAA website[10], or the NASA/GOES website[11]. GOES is the longest-operated solar-observing program in space and provides a basically continuous data stream of soft X-ray fluxes in the two 0.5-4 Å and 1-8 Å wavelength bands, which are widely used for the classification of solar flare magnitudes. The logarithmic flux values are labeled with letters (A, B, C, M, X-class), which denote the order of magnitude of the peak flux on a logarithmic scale ($A = 10^{-8}, B = 10^{-7}, C = 10^{-6}, M = 10^{-5}, X = 10^{-4} \, Wm^{-2}$), subdivided with an additional digit (e.g., an X2 class flare has a flux of 2×10^{-4} Wm^{-2}).

---

[10]http://www.oso.noaa.gov/goes/

[11]http://goespoes.gsfc.nasa.gov/project/index.html

Interball[12] is an international solar-terrestrial program to study the Earth magnetosphere with two spacecraft, one flying through the magnetospheric geotail (i.e., the *Tail Probe*, launched on 1995 August 3), and one flying over the polar aurora (i.e., the *Auroal Probe*, launched on 1996 August 29). One of the instruments onboard, RF15, comprises a solar photometer and an imager, designed for multi-band high-resolution measurements of the integral solar flux in the energy range between 2 keV and 240 keV as well as for imaging of solar flares in the 2-8 keV energy range. The X-ray imager has rotation-modulated collimators, similar to RHESSI, and thus is capable of Fourier imaging or solar flares (Sylwester et al. 2000).

TIMED-SEE[13] is the *Solar EUV Experiment (SEE)* instrument onboard the NASA *Thermosphere Ionosphere Mesosphere Energetics and Dynamics (TIMED)* mission, developed at the *Laboratory for Atmospheric and Space Physics (LASP)* at the University of Colorado, launched on December 2001. It studies solar irradiance and variability, in the VUV wavelength range of 0-200 nm, including the soft X-ray (XUV) range of 0-30 nm, the extreme-ultraviolot (EUV) range of 0-120 nm, and the far ultraviolet (FUV) range of 120-200 nm. TIMED/SEE data served for cross-calibration with SOHO/EIT irradiances (Hock and Eparvier 2008).

The *SMEI (Solar Mass Ejection Imager)*[14] is an instrument designed to detect the transient clouds of hot ionized gases that are launched by a *coronal mass ejection (CME)* from the solar surface and propagate through the entire interplanetary space and heliosphere. Of most interest are those CMEs that are directed towards Earth and have impacts on Earth-orbiting satellites, electrical power distribution networks, and long-distance radio communication. The SMEI spacecraft was launched on 2003 January 6, operated successfully for eight years, and stopped data-taking on 2011 September 28. SMIE data were used for tomographic reconstruction of the density enhancements associated with the propagation of interplanetary CMEs, in conjunction with interplanetary scintillation data, and provided information for space weather forecasting (Webb et al. 2002; Eyles et al. 2003; Jackson et al. 2004).

The *SOlar Radiation and Climate Experiment (SORCE)*[15] is a NASA-sponsored satellite, operated by LASP at the University of Colorado, dedicated to both solar and terrestrial observations, making measurements in X-rays, ultraviolet, visible, and near-infrared wavelengths, and total solar radiation. The SORCE measurements specifically address long-term climate changes, natural variability and enhanced climate prediction, and atmospheric ozone and UV-B radiation. The SORCE spacecraft was launched on 2003 January 25 and placed into a 645 km orbit with $40°$ inclination. SORCE continues to make precise measurements of the *total solar irradiance (TSI)*, which started with the *ERB* instrument in 1979 and has been continued to the present with the *ACRIM* series of measurements. SORCE provides also the solar spectral irradiance from 1 nm to 2000 nm, accounting for 95% of the spectral contribution to TSI. SORCE carries four instruments: the *Spectral Irradiance Monitor (SIM)*, the *Solar Stellar Irradiance Comparison Experiment (SOLSTICE)* (McClintock et al. 2005a,b; Snow et al. 2005a,b), the

---

[12]http://www.iki.rssi.ru/interball/
[13]http://lasp.colorado.edu/see/index.html
[14]http://www.sr.bham.ac.uk/ mpc/p2/smei/
[15]http://lasp.colorado.edu/sorce/index.htm

Total Irradiance Monitor (TIM) (Kopp et al. 2005), and the *XUV Photometer System (XPS)* (Woods and Rottman 2005; Woods et al. 2005; Woods et al. 2008). Technical documentations about SORCE are mostly given in the special issue of *Solar Physics* volume **230**, describing in addition the SORCE mission concept (Anderson and Cahalan 2005; Rottman et al. 2005; Pilewskie et al. 2005; Lean et al. 2005), the SORCE data system (Pankratz et al. 2005), and the spacecraft operations (Sparn et al. 2005).

SMART-1 (Small Missions for Advanced Research and Technology-1)[16] is a Swedish-designed ESA satellite that was launched on 2003 September 23 and orbited around the Moon, and was ended by a planned crash into the Moon's surface three years later, on 2006 September 3. Besides the new technology of a solar-powered Hall effect thruster propulsion system, SMART-1 carried out measurements to study chemical elements on the moon, solar variability, and the solar wind. SMART-1 was used for cross-calibration with GOES and RHESSI in soft X-ray wavelengths (Väänanen et al. 2009). The *D-CIXS (Demonstration of a Compact X-ray Spectrometer)* instrument (Huovelin et al. 2002, 2010) detected also the X-ray fluorescence of crystal componds created through the interaction of the electron shell with solar wind particles.

SOXS/GSAT-2 is a *Solar X-ray Spectrometer (SOXS)* instrument on board the Indian *Geostationary Satellite (GSAT-2)*, launched on 2003 May 8 (Vadher 2000; Jain et al. 2000, 2005). SOXS records the full-Sun hard X-ray flux from 4 keV to 10 MeV with comparable (spectral) energy resolution as RHESSI. Scientific results from the SOXS mission include the detection of the Fe-line feature at 6.4 and 6.7 keV during solar flares (Jain et al. 2006a,b, 2010), the energy-dependent timing of thermal emission in flares (Jain et al. 2011), and a study of microflares (Jain et al. 2006c).

SOLAR/SOLSPEC is one of three Sun-monitoring instruments on the external payload facility of the *International Space Station (ISS) Columbus*, measuring the total and spectral absolute irradiance from 16 nm to 3080 nm, launched on 2008 February 7 (Thuillier et al. 2009).

The *IRIS (Interface Region Imaging Spectrograph)*[17] is a NASA-sponsored solar space mission to be launched in April 2013, containing a multi-channel imaging spectrograph with a 20 cm UV telescope, capable of obtaining spectra along a slit (0.3″ wide) and slit-jaw images. The primary objectives of the IRIS mission is the exploration of the interface between the solar chromosphere, transition region, and corona, in order to understand how the plasma flows generated by the internal magneto-convection drives coronal activity:

1. Which types of non-thermal energy dominate in the chromosphere and beyond?

2. How does the chromopshere regulate mass and energy supply to corona and heliosphere?

3. How do magnetic flux and matter rise through the lower atmosphere, and what role does flux emergence play in flares and coronal mass ejections?

---

[16]http://en.wikipedia.org/wiki/SMART-1
[17]http://science.nasa.gov/missions/iris/

Figure 1.14: HIREGS large balloon-borne X-ray and gamma-ray detectors to observe solar flares and astrophysical high-energy sources, launched by the Univ. Berkeley Space Physics Research Group (principal investigator Bob Lin), circum-navigating Antarctica from November 1994 to January 1995 (Credit: Univ. Berkeley SPR).

Suborbital Rocket Flights provide only short-interval trajectories into the upper atmosphere, typically lasting about 7 min, during which a short, well-planned, one-time measurement in space can be made. Solar rocket flights served mostly for testing new technologies, as a proof of concept for major space-borne missions to follow. Some of the notable solar rocket flights during the beginning of the 21st century include: two SWRI/LASP sounding rocket flights launched on 1997 May 15 and 1998 November 2 provided inter-calibration with the EUV imagers on SOHO and TRACE (Auchere et al. 2001); the *MOSES (Multi-Order Solar EUV Spectragraph)* sounding rocket payload, built by Univ. Montana, flown on 2006 February 8, which demonstrated multi-order EUV tomography (Kankelborg 2001a,b, 2006); the *Solar XUV Doppler Telescope (XDT)* flown by ISAS on 1998 January 31, which demonstrated Doppler shift maps of the Fe XIV 211 Å line (Kano et al. 2000; Kobayashi et al. 2000); the *EUNIS-06* and 07 missions with a EUV normal-incidence spectrometer, first proposed by Thomas and Davila (2001), flown on 2006 April 12 and 2007 November 6, which provided absolute radiometric calibration in the wavelength band of 170-205 Å (Wang et al. 2010) and cross-calibration with SOHO/CDS and Hinode/EIS (Wang et al. 2011); the *Hi-C* sounding rocket flight on 2012 July 11, which carried a 0.2″EUV imager and revealed spatially resolved magnetic braids in the solar corona with unprecedented spatial resolution (Cirtain et al. 2013).

Balloon flights: Balloon-borne telescopes have been flown to test detectors in wavelengths that are absorbed by the lower Earth's atmosphere (hard X-rays, soft X-rays, EUV) or to test telescopes in optical wavelengths with a superior atmospheric seeing compared with ground-based telescopes. Although some balloon flights have been conducted at low geographic latitudes (e.g., at NASA's Scientific Balloon Facility in Pales-

tine, Texas), the preferred route for long-duration ballons is circling Antarctica, where the air is very dry (yielding an optimum seeing at low moisture) and balloons return to the same launch site after a 2-3 week period. Ultra-long-duration balloon flights up to 100 days over Antarctica and Artcic are anticipated to provide full annual coverage and lower cost than a space-borne payload (Smith 2004). We briefly mention a few balloon flights with solar instrumentation. The *HIREGS* payload with hard X-ray and gamma-ray detectors, designed to detect solar and astrophysical high-energy radiation, was flown by the University of Berkeley Space Physics Research Group from November 1994 to January 1995 (Fig. 1.14). An 80-cm Ritchey-Chretien solar telescope *GENE-SIS* that acquired long time series of high spatial resolution (diffraction-limited $0.2''$) and vector magnetograms was flown in January 2000 for 17 days in the stratosphere above Antarctica (Bernasconi et al. 2000), studying also the magnetic topology of so-called *Ellerman bombs* (Schmieder et al. 2002). A Japanese balloon-borne hard *X-ray Doppler Telescope (XDT)* to obtain high-resolution spectra (with 3 keV resolution) of solar flares over the energy range of 15-120 keV was flown on 2001 August 29 and 2002 May 24, detecting an M1.1 flare (Kobayashi et al. 2002, 2003, 2004). The largest optical telescope flown on a balloon is the (German built) 1-m aperture Gregory tele-scope SUNRISE, which was launched on 2009 June 8 near Kiruna in northern Sweden and floated westward to land on Somerset island in northern Canada on 2009 June 13 (Solanki et al. 2010; Barthol et al. 2011). The SUNRISE telescope carried a UV fil-ter imager and an imaging vector polarimeter (IMAX). The numerous scientific results obtained on the photospheric dynamics observed during this balloon flight are docu-mented in over 20 publications in the special issue of *The Astrophysical Jorunal Letters* volume **723**.

Future Solar Mission Concepts: Prospects of future solar space missions will un-doubtly continue in the "solar renaissance era" in which we are living at the beginning of the 21st century (Fleck and Marsden 2002). One of the upcoming major solar mis-sions is built by ESA, the *Solar Orbiter*[18], which will explore the Sun from a unique orbit that brings the probe to within 0.21 AU to the Sun and to solar latitudes as high as $38°$, carrying a battery of remote-sensing and in-situ instruments, expected to be launched in 2017 (Fleck et al. 2001; Fleck and Marsden 2002; Martens and Kankel-borg 2001; Marsden 2003; Woch and Gizon 2007; Mueller et al. 2012).

Direct hard X-ray imagers with focusing optics is a new concept that provides higher spatial resolution and a much higher dynamic range than traditional Fourier imagers (Dennis et al. 2012). One prototype, the *Focussing Optics X-Ray Solar Im-ager FOXSI* had a successful rocket flight on 2012 November 16 and demonstrated a hard X-ray imaging quality superior to RHESSI (Krucker et al. 2009, 2011).

One of the longest proposed missions is the *Solar Probe*[19], which should approach the Sun as close as 8.5 solar radii (0.034 AU), but a launch date is not scheduled before 2018.

Other proposed ideas of future solar missions focus on the solar magnetism from the solar surface to space weather (*DynaMICCS*: Turck-Chieze et al. 2009a,b), a spectro-polarimetrtic EUV imager with an occulter on two spacecraft in formation flight (*SolmeX*:

---

[18]http://en.wikipedia.org/wiki/Solar_Orbiter
[19]http://en.wikipedia.org/wiki/Solar_Probe_Plus

Figure 1.15: The Nobeyama Radioheliograph (NoRH) in Japan, consisting of 84 parabolic antennas with 80 cm diameter, arranged in two arms, one with a length of 490 m in east/west direction, the other with a length of 220 m in north-south direction. First observations were made in April 1992, and are continued already over 20 years (Credit: NRO/NAO).

Peter et al. 2011, 2012), a VUV imaging spectrograph for the JAXA Solar-C mission (*LEMUR*: Korendyke et al. 2011), imaging X-ray polarimetry of solar flares on a balloon payload (*IXPS*: Hosack et al. 2011), a solar particle acceleration radiation and kinetics mission (*SPARK*, Matthews et al. 2012), a *Earth-Affecting Solar Causes Observatory (EASCO)* in the Langrangian point L5 (Gopalswamy et al. 2011), or solar radio observations from lunar sites (Lazio et al. 2011).

1.8 Radio Instrumentation

Solar observations in radio wavelengths can be made with ground-based instruments, since the atmosphere is transparent in the radio band. First solar radio observations have been pioneered by Grote Reber as early as 1942, while the first solar radiospectrograph has been built at Penrith (Australia) in 1948 (Steward et al. 2010). Since about 1970, a large number of radio spectrometers were built around the world and some are still in use for solar observations. A major breakthrough was the advent of radio interferometers, which came online since about 1980, such as the *Very Large Array (VLA)*, the *Owens Varlly Radio Observatory (OVRO)*, the French *Nançay Radioheliograpn*, the Russian *Ratan-600*, or the Japanese *Nobeyama Radioheliograph* (Fig. 1.15), which are all still in use at the time of writing. In Table 1.5 we list the currently operating solar-observing radio interferometers. A more complete list of (radio and optical)

Table 1.5: Solar-observing radio interferometers operational at the beginning of the 21th century.

Acronym	Instrument name and location	Frequency range	Imaging angular resolution
VLA	Very Large Array, New Mexico	80 MHz-4.3 GHz	0.05-700″
OVSA	Owens Valley Solar Array, California	1-18 GHz	7-128″
NoRH	Nobeyama Radioheliograph, Japan	17, 34 GHz	8-16″
NRH	Nançay Radioheliograpn, France	164-432 MHz	120-300″
RATAN-600	Special Astrophysical Observatory, Russia	1-7 GHz	12-235″
SSRT	Siberian Solar Radio Telescope, Irkutsk	5.7 GHz	15″
GRH	Gauribidanur Radioheliograph, India	30-110 MHz	300″
BDA	Brazilian Decimetric Array, Brazil	1.2-1.7 GHz	90″

ground-based observatories can be found on the *Max Millenium Program* website[20].

The *Very Large Array (VLA)*[21] is the most powerful radio instrument regarding imaging quality, spatial resolution, and frequency range (metric, decimetric, microwaves), but since it is not solar-dedicated, solar flares are caught only rarely during the sparsely allocated observing time intervals of a few hours.

The *Owens Valley Solar Array (OVSA)*[22], operated by the *New Jersey Institute of Technology (NJIT)*, is a solar-dedicated radio interferometer that is designed to image solar flares and active regions in microwaves. The ongoing OVSA expansion project complements the currently operating 7 antennas to a total of 15, in the frequency range of 1-18 GHz. Automated localization of solar flares is accomplished with the *Solar Radio Burst Locator (SRBL)* capability (Dougherty et al. 2000; Gallagher et al. 2000, Hwangbo et al. 2005),

The *Nobeyama Radioheliograph (NoRH)*[23] (Fig. 1.15) is the major workhorse of solar radio imaging during the last decade, and completed 20 years of service in 2012. The solar-dedicated NoRH consists of 84 dishes with a maximum baseline of 490 m in east/west direction, operating daily 8 hours since 1992. The NoRH produces full-Sun images, capturing active regions, flares, prominences, coronal mass ejections, and has even sufficient time resolution (0.1-1.0 s) to resolve rapid dynamic phenomena, such as flare loop oscillations.

The *Nançay Radioheliograph (NRH)*[24] is also a long-operating facility that images the Sun at 164, 236, 327, 410, and 432 MHz on a daily basis. The NRH has also the capability of flare multi-channel imaging with sub-second time resolution, which allows it to image the trajectories of type III bursts and coronal mass ejections.

---

[20]http://solar.physics.montana.edu/max_millennium/obs/GBO.html

[21]http://www.vla.nrao.edu/

[22]http://www.ovsa.njit.edu/

[23]http://solar.nro.nao.ac.jp/

[24]http://secchirh.obspm.fr/nrh.php

RATAN-600[25] is a circular array of reflectors that provides high spatial resolution in one scan dimension, in a large number (52) of frequency channels, which makes it ideal for frequency-tomography of active regions. 2D-image reconstruction with RATAN-600 data has been faciliated (Golubchina et al. 2002), and recent upgrades in data processing are described in Baldin et al. (2011).

The *Siberian Solar Radio Telescope (SSRT)*[26] provides 2D imaging of the Sun at 5.7 GHz and can switch to a very high time resolution of 56 ms during a flare mode. The current status and upgrades with a future SSRT-based radio heliograph are described in Grechnev et al. (2003) and Lesovoy et al. (2009).

First solar observations with the *Allen Telescope Array (ATA)*[27] interferometer, the first *widefield, panchromatic, snapshot radio camera for radio astronomy and SETI* (Welch et al. 2009), located near Hat Creek (California), have demonstrated high-quality mapping of the Quiet Sun from 1.43 GHz to 6 GHz (Saint-Hilaire et al.2012).

Other radio interferometers came online in Gauribidanur (India)[28] in the low frequency range of 40-150 MHz (Ramesh et al. 2006, 2008), the *Brazilian Decimetric Array (BDA)* in the 1.2-1.7 GHz range (Sawant et al. 2000, 2003, 2007, 2011), and further instruments are planned in Mongolia, Inner China (Yan et al. 2009).

The *Low-Frequency Array (LOFAR)*[29], built by the Netherlands astronomical foundation ASTRON, is the largest connected radio telescope using an array of about 20,000 small omni-directional antennas, distributed across the Netherlands, Germany, Great Britain, France, and Sweden. Initial LOFAR test stations became operational since 2003, and about 40 stations became operational by 2012. Although this array is mostly dedicated to astrophysical observations of extragalactic and cosmological sources, solar physics and space weather is also an item to be pursued (White et al. 2003; Bastian 2004; Cairns 2004; Oberoi and Kasper 2004).

The *Atacama Large Millimeter Array (ALMA)*[30] is located in the Atacama desert in Chile, where the very dry air conditions allow measurements in mm and sub-mmm wavelengths. The ALMA array consists of 66 radio dishes (with 7 and 12 m diameter) and began scientific observations in 2011, expected to be fully operational in 2013. The primary science objectives are star birth during the early universe and detailed imaging of local star and planet formation, but ALMA is also thought to be an ideal probe of the solar chromosphere (Loukitcheva et al. 2008).

The *Frequency Agile Solar Radiotelescope (FASR)*[31] is a planned ultra-wideband radio array designed to image the Sun and its atmosphere (from the chromosphere to the corona) over a frequency range of 50 MHz to more than 20 GHz (corresponding to wavelengths from 6 m down to 1.5 cm). The multi-frequency imaging technique allows 3D frequency tomography of solar active regions, flares, and CMEs. The FASR project is managed by a consortium that includes NJIT and NRAO, and a reduced prototype version is currently installed and tested at OVSA (Bastian 2003a,b,c, 2004; Gary and

---

[25] http://www.sao.ru/ratan/

[26] http://ssrt.iszf.irk.ru/

[27] http://ral.berkeley.edu/ata/

[28] http://www.iiap.res.in/centers/radio

[29] http://www.lofar.org

[30] http://www.almaobservatory.org/

[31] http://www.fasr.org/

Keller 2003; Gary 2004; White et al. 2003; Liu et al. 2007).

Besides solar radio interferometry that provides images of the Sun, there are a number of radio spectrometers in operation, which all switched from the analog recording technology of the last millenium to digital dynamic spectra, which display frequency spectra as a function of time with high time resolution. A world-wide net of solar radio spectrometers, called *e-CALLISTO (Compound Astronomical Low-cost Low-frequency Instrument for Spectroscopy in Transportable Observatory)*[32] has been created, which consists of identical programmable heterodyne receivers, connected through the internet, operating in the 45-870 MHz decimetric range (Benz et al. 2005, 2009). Host observatories of e-CALLISTO are in: Bleien near Zürich (Switzerland), Effelsberg (Germany), Humain (Belgium), the *Rosse Solar Terrestrial Observatory (RSTO)*[33] in Birr Castle (Ireland) (Zucca et al. 2012), Glasgow (UK), Metsähovi (Finland), Ondrejov (Czech Republic), Trieste (Italy), Hurbabova (Slovakia), Crimea (Ukraine), Badary (Russia), Ulan Bator (Mongolia), Almaty (Kazakhstan), Sri Lanka, Kuala Lumpur (Malaysia), Daejeon (South Korea; Bong et al. 2009), Gauribidanur, Ooty, and Pune (India), Helwan (Egypt), Poste de Flacq (Mauritius), Hawaii (USA), Anchorage (Alaska USA), Mexico City (Mexico), San Jose (Costa Rica), Cachoeira Paulista (Brazil), Perth and Melbourne (Australia), Nairobi (Kenja).

Other new developments (after 2000) of solar radio spectrometers include: the *Ichon Solar Radio Spectrograph* in Korea, operating in the 30-2500 MHz frequency range and designed to track type II bursts during CMEs (Cho et al. 2003; Choi et al. 2005), the Chinese *Solar Broadband Radio Spectrometer (SBRS)* operating in frequency bands from 0.7 to 7.6 GHz with antennas in Bejing, Kunming, and Nanjing (Ji et al. 2003, 2005; Xu et al. 2003; Fu et al. 2004; Fang 2011), the *ARTEMIS IV* solar radio spectrograph with a frequency range of 20-650 MHz, operating at Thermopylae, Greece (Alissandrakis et al. 2009), and the high-sensitivity *Assembly of Metric-band Aperture TElescope and Real-time Analysis System (AMATEROS)* of Tohoku University in Japan (Iwai et al. 2012).

What are the major contributions of solar radio observations to the physics of the solar corona over the last decade? Scanning the most-cited papers we find the following topics: A statistical study on prominence eruptions and coronal mass ejections, using Nobeyama observations (Gopalswamy et al. 2003), X-ray and radio observations of a large-scale solar coronal shock wave, using Nançay imaging data and Potsdam radio spectra (Khan and Aurass 2002), fast MHD sausage mode quasi-periodic oscillations in coronal loops (Nakariakov et al. 2003), direct imaging of a coronal mass ejection with the Nançay Radioheliograph (Bastian et al. 2001), the magnetic reconnection rate in the decay phase of a long-duration flare (Isobe et al. 2002), the evolution of coronal mass ejections in the early phase (Gopalswamy and Thompson 2000), first imaging of quasi-periodic pulsations related to the acceleration of gyro-synchrotron producing electrons during solar flares (Asai et al. 2001; Melnikov et al. 2005), loop-top nonthermal microwave emission associated with the acceleration region of solar flare loops (Melnikov et al. 2002); radio imaging of type II and type III bursts with the Nançay

---

[32]http://www.e-callisto.org/
[33]http://www.rosseobservatory.ie

Radioheliograph of 30-500 keV electrons that escape into interplanetary space and in-situ detected with the *Wind* spacecraft (Klein et al. 2005), imaging of the Bastille-day (2000 July 14) coronal mass ejection with the Nançay Radioheliograph and the Ooty Radio Telescope (Manoharan et al. 2001), converging motion indicating the fast relaxation of sheared magnetic fields during a solar flare (Ji et al. 2006), hard X-ray radiation from a fast coronal ejection (Hudson et al. 2001), statistical studies of solar flare radio spectra obtained with OVSA (Nita et al. 2004), solar microwave bursts and injection pitch-angle distribution of flare electrons (Lee and Gary 2000), hard X-ray and OVSA microwave observations of microflares (Qiu et al. 2004), or microwave tomography of solar magnetic fields with RATAN-600 (Grebinskij et al. 2000). The most significant solar observations in radio wavelengths are clearly made by interferometers with good imaging quality, but non-imaging radio spectrometers often provide very useful information on the origin and propagation of non-thermal electrons, which can be traced from their plasma emission and gyro-synchrostron emission.

1.9 Optical and Infrared Instrumentation

Last but not least, we will give also an overview of ground-based solar observatories and instrumental capabilities in optical and infrared wavelengths that substantially contributed to a better understanding of the physics of the solar corona during the last decade. Since the scope of this book is on the solar corona, photospheric and chromospheric observations are not covered here, unless there is a direct connection with coronal phenomena. Complementary articles can be found, e.g., on the history of solar telescopes (Von der Lühe 2009), on innovative telescopes and instrumentation for solar astrophysics (Keil and Avakyan (2003), or on adaptive optics (Rimmele and Marino 2011),

A list of major optical solar telescopes[34] that are currently operating or in construction is given in Table 1.6. Some of the new instrumental developments over the last decade include, in chronological order: the control system for the *Synoptic Optical Long-term Investigations of the Sun (SOLIS)* at KPNO (Goodrich 2000; Wampler 2000), which produces synoptic magnetic maps of the Sun; the SOLIS vector spectromagnetograph (VSM) (Jones et al. 2002), upgrades of the Fabry-Perot interferometer TESOS at VTT (Tritschler et al. 2002); the *Dutch Open Telescope* (Rutten et al. 2002; Hammerschlag et al. 2009); the *Multi Channel Subtractive Double Pass (MSDP)* of THEMIS (Mein 2002; Briand and Ceppatelli 2002; Gelly et al. 2008), solar polarimetry in near-UV with the Zürich Imaging Polarimeter ZIMPOL II, operated at the *Istituto Ricerche Solari LOcarno (IRSOL)* in Switzerland (Gandofer et al. 2004); the development of the Goettingen Fabry-Perot spectrometer for GREGOR (Puschmann et al. 2006), the *Spectro-Polarimeter for Infrared and Optical Regions (SPINOR)* for the Dunn Solar Telescope at NSO (Socas-Navarro et al. 2006); the (new) Big Bear Solar Observatory's digital vector magnetograph with a 160 cm aperture (Goode et al. 2003; Didkovsky et al. 2004; Denker et al. 2006); Stokes imaging polarimetry using image restoration at the *Swedisth 1-m Solar Telescope (SST)* (VanNoort et al. 2008),

---

[34]http://en.wikipedia.org/wiki/List_of_solar_telescopes

Table 1.6: A selection of currently operating large optical solar telescopes.

Acronym	Telescope name	Aperture	Year	Location
ATST	Advanced Technology Solar Telescope	424 cm	...	Maui, US
GREGOR	GREGOR solar telescope	150 cm	2012-	Tenerife, Spain
BBSO	Big Bear Solar Observatory	160 cm	2008-	Big Bear, US
SST	Swedish 1-m Solar Telescope	100 cm	2002-	La Palma, Spain
DOT	Dutch Open Telescope	45 cm	1997-	La Palma, Spain
THEMIS	THEMIS Solar Telescope (French)	90 cm	1996-	Tenerife, Spain
VTT	Vacuum Tower Telescope (German)	70 cm	1989-	Tenerife, Spain
DST	Dunn Solar Telescope	152 cm	1969-	Sacramento Peak
KPNO	McMath-Pierce Solar Telescope	161 cm	1961-	Kitt Peak, US

straylight characterization in the post-focus imaging instrumentation of SST, and comparison with the *CRISP* Imaging SpectroPolarimeter) (Loefdahl and Scharmer 2012), the Tenerife Infrared Polarimeter II (Collados et al. 2007), a polarization model for the German *Vaccumm Tower Telescope (VTT)* (Beck et al. 2005), the KIS/IAA *Visible Imaging Polarimeter (VIP)*, a post-focus instrument that upgrades the TESOS spectrometer at the VTT (Beck et al. 2010); the *Rapid Oscillations in the Solar Atmosphere (ROSA)* high-cadence, synchronized multi-camera (Jess et al. 2010), and the *Interferometric Bidimensional Spectrometer (IBIS)* at the Dunn Solar Telescope with the *Spectro-Polarimeter (SP)* (Cavallini 2006; Reardon and Cavallini 2008; Righini et al. 2010). The next major optical solar facility is the *Advanced Technology Solar Telescope (ATST)* (Keil et al. 2004), which is currently under construction on the Hawaiian island Maui, where optimum seeing was measured (Lin and Penn 2004). Two workshops on prospective ATST science have already been held (Pevtsov and Uitenbroek 2002; Rimmele et al. 2012).

What is the significance of optical and infrared observations from ground-based telescopes to the understanding of the physics of the solar corona? In the following we outline a few topics of solar corona physics, based on the most frequently cited publications, that have been pursued over the last decade.

Solar Eclipse Observations: Solar eclipses observations (Fig. 1.16), the only natural method to see the faint corona without being blinded by the six orders of magnitude brighter photosphere in optical light, still produces high-quality science results, although we observed solar eclipses since millenia. Some of the most cited results during the last decade deal with: the magnetic origin of ray-like fine structure of the white-light corona (Wang et al. 2007), eclipse observations of high-frequency oscillations in active region loops (Katsiyannis et al. 2003), a new numerical method of total solar eclipse photography processing (Druckmüller et al. 2006), the *Solar Eclipse Coronal Eclipse Imaging System (SECIS)* (Phillips et al. 2000), the mapping of the distributon of electron temperature and Fe charge states during eclipses (Habbal et al. 2010a), or eclipse observations of hot prominence shrouds (Habbal et al. 2010b).

Coronagraphic Observations: Solar coronagraphs mimic natural solar eclipses by

Figure 1.16: The solar eclipse of 2012 May 20 observed in Doyle, California. The time sequence illustrates the flashing-up of the solar corona during the totality, which is not visible at other times due to the immense brightness contrast (Credit: Public Website).

blocking out the bright visible light from the photospheric disk by an occulting disk, invented by Bernard Lyot in 1930. In order to eliminate the Rayleigh-scattered light in the Earth's atmosphere, ground-based coronagraphs are using the polarization to distinguish the (unpolarized) sky brightness from the polarized light of the corona, which is produced by near-perpendicular Thompson-scattering. Space-based coronagraphs are LASCO on SOHO, and COR-1 and COR-2 on STEREO. One of the most used ground-based instruments is the *Mark IV Coronagraph* operated by the *High Altitude Observatory (HAO)* on top of Mauna Loa, Hawaii. Mark IV Coronagraph observations helped to reconstruct the geometry of magnetic reconnection sites (Lin et al. 2005), CME-associated current sheets (Ko et al. 2003; Ciaravella and Raymond 2008), or the initiation of a CME (Bemporad et al. 2007).

Coronal Magnetometry: Measuring the magnetic field in the solar corona is a very important task, but current capabilities are very limited. A feasibility study of coronal magnetometry (Judge 2001) recommends more dedicated instruments that measure the weak Zeeman-induced Stokes V signal in the Fe XIII line (10,746 Å) and the Hanle effect in the He I line (10,830 Å). Some first full-Stokes spectro-polarimetric measurements of the forbidden Fe XIII coronal emission line yielded field strenths of $B \approx 4$ G at an altitude of $100''$ above the solar limb (Lin et al. 2004). The *Advanced Technology Solar Telescope (ATST)* will have the capabilities to measure the magnetic field with high resolution in the photosphere (Fe I, 6303 Å and Mg I, 12,320 Å lines) and chromosphere (Ca II 8542 Å). Magnetic fields in the solar corona and solar wind

are generally extrapolated from photospheric magnetograms or vector field data, but these methods suffer from the non-force-freeness of the photosphere and insufficient knowledge of the magnetic field at the boundaries of the computation box (DeRosa et al. 2009). Improved *nonlinear force-free field (NLFFF)* extrapolations in spherical geometry have been conducted with boundary data treatment applied to the vector spectro-magnetograpn (VSM) data of the SOLIS instrument from KPNO (Tadesse et al. 2011). Alternatively, using EUV images instead of optical magnetograms, the coronal magnetic field can also be calculated from analytical NLFFF approximations fitted to the geometry of stereoscopically triangulated loops (with known 3D geometry) or loops traced in EUV images (with known 2D geometry) (Aschwanden 2013). During the launch of a CME, the magnetic field in the corona can also be derived from the Alfvénic Mach number of CME shock fronts, using EUV images (Gopalswamy et al. 2012). And during flares, if oscillating loops are present, the magnetic field can also be inferred from coronal seismology (Roberts 2000; Nakariakov and Verwichte 2005).

Coronal Loop Oscillations and Propagating Waves: There are a number of quasi-periodic coronal phenomena that have been detected in optical wavelengths, associated with standing oscillations or propagating waves in coronal loops. Early detections were made with the Sacramento Peak coronagraph (Koutchmy et al. 1983), during the eclipses in Hydrabad (Pasachoff and Landman 1984), in East Java (Pasachoff and Ladd 1987), in Chile (Pasachoff et al. 2000), in Romania (Pasachoff et al. 2002), with the Norikura coronagraph (Sakurai et al. 2002), with the SECIS equipment during the eclipse in Bulgaria (Williams et al. 2001, 2002), during the eclipse in Anji, China (Singh et al. 2011), with SOHO/UCVS in the outer corona (Ofman et al. 1997, 2000), and most spectacularly in the 10,747 Å and 10,798 Å line with the *Coronal Multi-channel Polarimeter (CoMP)*[35] at the NSO's Sacramento Peak Obsevatory (Tomczyk et al. 2007; Tomczyk and McIntosh 2009). The latter observations of oscillations or waves by Tomcyk et al. (2007) were found to be ubiquitous in the solar corona, although at such a small amplitude level that the waves can only be detected in Doppler shift, rather than from the spatial oscillation amplitude. Nevertheless, these observations in white light have spawned a broad discussion about the interpretation in terms of MHD fast-mode kink oscillations, Alfvénic waves, propagating waves, or quasi-periodic flows.

Coupling of Photospheric and Coronal Phenomena: Like the Earth's oceans generate water moisture in the air, winds, and rain clouds, which dictate the weather in the atmosphere, the solar photosphere and chromosphere are the reservoirs of many coronal phenomena, which can only be understood by studying both the photospheric origins and the coronal consequences as an integrated system. White-light observations reveal to us the sub-photospheric magneto-convection, magnetic flux emergence, the magnetic field evolution on the solar surface, but also the build-up of non-potential magnetic energy in form of sheared and twisted fields, which leads to eruptive filaments, flares, and coronal mass ejections. There are a number of solar phenomena that reveal a coupling between the photosphere, chromosphere, and corona, such as: acoustic shocks, spicular upflows, soft X-ray jets, explosive events, Ellerman bombs,

---

[35]http://www.cosmo.ucar.edu/COMP.html

chromospheric evaporation, nanoflares, bright points, etc. A key question is which of these mostly small-scale variabiliy phenomena contribute to coronal heating. The observational verification of coupled phenomena between the chromosphere and corona requires high spatial and temporal resolution in many wavelengths. One suitable instrument for this task is the *Rapid Oscillations in the Solar Atmosphere (ROSA)* high-cadence, synchronized multi-camera solar imaging system, currently operated at the Dunn Solar Telescope at NSO (Jess et al. 2010). The space-based *Interface Region Imaging Spectrograph (IRIS)*, containing a multi-channel imaging EUV spectrograph has a complementary function to disentangle the interface between the solar chromosphere, transition region, and corona. And all the options that ATST will provide in this endeavour are discussed in the proceedings of the 2nd ATST-EAST Meeting on *Magnetic Fields from the Photosphere to the Corona* (ASP volume **463**; Rimmele et al. 2012.).

1.10   Summary

In this first chapter we familiarize ourselves with new or upgraded instrumentation in solar corona physics that became available or was operational during the first decade of the 21st century, while the pre-2000 era was covered in Volume 1 of the book "Physics of the Solar Corona. An Introduction". We start our overview with a timeline of space-borne solar-dedicated missions and point out the trend of exponential growth in computer capacity (Moore's Law) and publication volume that characterizes and shapes the current era of solar physics (Section 1.1). We describe the instrumental capabilities of the major solar space missions, namely the RHESSI mission (Section 1.2), the STEREO mission (Section 1.3), the Hinode mission (Section 1.4), and the SDO mission (Section 1.5), and describe the scientific output of these flagship missions in the format of officially formulated mission goals, and somewhat more empirically, by singling out 10 top-rated scientific highlights or discoveries, mostly selected by the criterion of the highest citation rates at the time of writing. Besides these major solar observatory missions built by the US, European, or Japanese space agencies, we cover also the Russian series of CORONAS missions (Section 1.6), ancillary space missions with solar capabilities, suborbital sounding rocket flights, and balloon-borne experiments (Section 1.7). The ground-based solar observing capabilities in radio wavelengths (Section 1.8) and white-light or infrared (Section 1.9) are described separately, in particular with respect to their contributions to solar coronal physics. This cursory overview of solar instrmentation and novel scientific results given here in chapter 1 serves only as a starting point for a much more detailed discussion of the underlying physics to follow in the subsequent chapters.